Progress In Electromagnetics Research B, Vol. 94, 75–103, 2021

A Review of Metasurface-Assisted RCS Reduction Techniques

Akila Murugesan[1], Krishnasamy T. Selvan[1, *], Ashwin K. Iyer[2], Kumar V. Srivatsav[3], and Arokiaswami Alphones[4]

Abstract—This review discusses the evolution of the various radar cross-section (RCS) reduction techniques, with an emphasis on metasurfaces. The paper first introduces the terms RCS and RCS reduction and then discusses conventional and modern techniques to reduce RCS. The two main strategies used are scattering and absorption. The traditional methods of shaping and Radar Absorbing Material (RAM) are first briefly reviewed, followed by an extensive review of metasurface-based RCS reduction. RCS-reducing metasurfaces have the unique characteristics of acting as scatterers and absorbers. They are also described with regard to their passive and active configurations. The paper discusses RCS reduction techniques with respect to profile, bandwidth, angular stability, polarization sensitivity, design complexity, and cost-effectiveness. A comprehensive comparison chart based on the performance parameters such as bandwidth, size and angular stability is tabulated for the different types of metasurfaces. The review also details areas that require further investigation.

1. INTRODUCTION

The IEEE dictionary [1] defines RCS as 4π times the ratio of the power per unit solid angle scattered in a specified direction to the power per unit area in a plane wave incident on the scatterer from a specified direction. The RCS of a target depends on the frequency and polarization of the electromagnetic wave and its angle of incidence, as well as on the geometry, material properties, and shape of the target itself. RCS is classified as either monostatic or bistatic based on the transmitter and receiver positioning, as described in Figure 1. Monostatic corresponds to the measure of RCS when the transmitter and receiver are at the same location. In the case of bistatic, the transmitter and receiver are placed at different locations.

RCS reduction refers to reducing the visibility of the target by radar. Ideal RCS reduction refers to the non-detectability of the target regardless of the incident wave's frequency, angle of incidence, or polarization. However, such ideal RCS reduction is not practically realizable. An RCS reduction of 10 dB is usually considered adequate for practical purposes [2]. Obtaining a 10 dB RCS reduction for any target corresponds to a 90% reduction in the radar cross-section. Enhancing the RCS reduction bandwidth has been the subject of intense focus in recent times.

RCS reduction of targets is essential in civil and military applications. Military application of RCS reduction in stealth has its root in World War I, where cellulose-based material was used to reduce the detectability of military weapons and aircraft. In World War II, a wooden covering was used to obtain low observability of the Horten 229 V3 aircraft [3]. High dielectric constant materials were also used. The Russian scientist PyotrUfimstev [4] proposed an approximate method to calculate the scattering of electromagnetic waves from different objects. Researchers from Lockheed Martin used his ideas to

Received 14 August 2021, Accepted 3 October 2021, Scheduled 8 November 2021
* Corresponding author: Krishnasamy T. Selvan (selvankt@ssn.edu.in).
[1] Sri Sivasubramaniya Nadar College of Engineering, Kalavakkam 603110, Chennai, India. [2] University of Alberta, Edmonton, Alberta, Canada. [3] Indian Institute of Technology, Kanpur 208016, Uttar Pradesh, India. [4] Nanyang Technological University, Singapore.

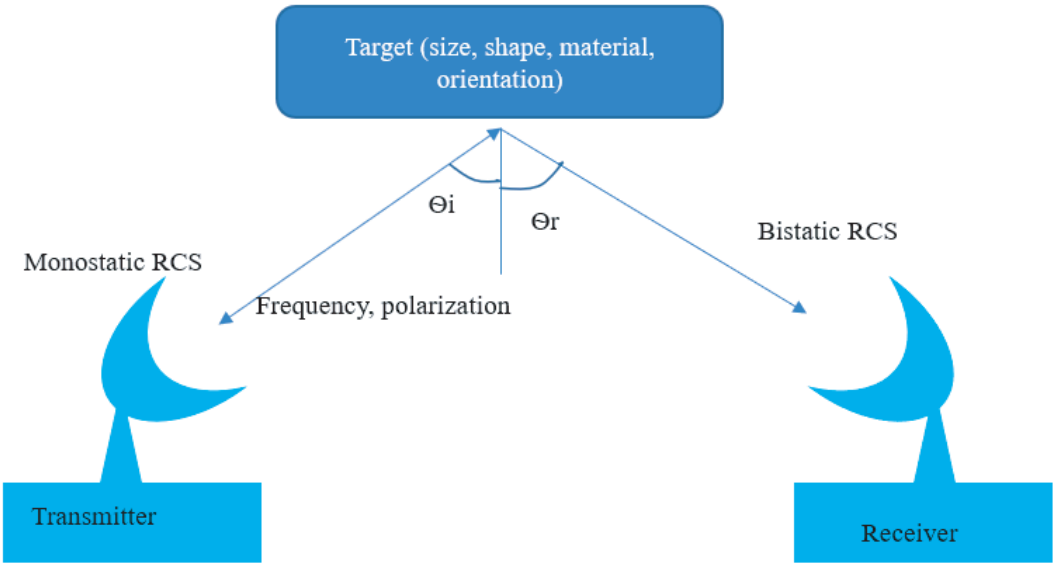

Figure 1. Monostatic and bistatic RCS.

develop the stealth aircraft SR-71 [5]. This spy plane had an unusual shape and was coated with absorptive paint, thereby reducing the RCS.

Two fundamental mechanisms used to achieve RCS reduction are scattering and absorption. Scattering deflects the incident signal away from the radar, while absorption dissipates all or part of the incident wave in an absorbing layer. Shaping is one method that works via the scattering mechanism, while radar-absorbing material (RAM) works via absorption. Both methods have been in use since stealth technology evolved, but in recent times metasurfaces have become ubiquitous in this area owing to their superior characteristics. A metasurface is a periodic or aperiodic array of subwavelength resonant scatterers that influence the electromagnetic response of the surface [6]. The fundamental blocks of the metasurface are the subwavelength scatterers that change the magnitude, phase, and polarization of the incident wave. Appropriate design of the subwavelength scatterers and their placement in the array yields the desired outcomes, paving the way for a variety of applications. Several review papers such as [7–12] and [13] have comprehensively discussed metamaterials/metasurfaces (MTM/MTS) and their applications. Metasurfaces used for RCS reduction can be based on both scattering and absorption. A critical review of RCS-reducing metasurfaces is provided in this paper, in addition to a brief discussion of the conventional methods of shaping and radar-absorbing materials.

The various approaches proposed for RCS reduction in the literature can be brought under either one of the two broad categories, namely scattering and absorption. Therefore, this article will examine these two categories and elaborate on the traditional and the current technology of reducing RCS within each subcategory. As the main focus of the paper is on metasurfaces, the classification section briefly discusses the traditional methods of reducing RCS.

This paper is structured as follows. Section 2 discusses the applications of RCS reduction. In Section 3, a comprehensive classification of RCS reduction approaches is provided, along with a brief overview of the traditional methods. Scattering-based metasurfaces are discussed in Section 4, while absorption-based metasurfaces are discussed in Section 5. Section 6 identifies topics that require further examination, and Section 7 concludes the paper.

2. APPLICATIONS OF RCS REDUCTION

Radars are used in a wide variety of applications. They are used to track aircraft and ships, detect insects [14] and animals, measure automobiles' speed [15], and predict weather conditions. RCS is the measure of the electromagnetic signature of an object measured using radars. Though detectability of

the objects is essential in specific scenarios such as intelligent vehicular navigation, track aeroplanes and ships, there are certain situations where the objects should have low detectability. These are mentioned below.

(i) One application of RCS reduction is in aircraft hangars [16]. Aircraft hangars are parking decks of aircraft. When located near airports, the signal reflected from the hangars interferes with the aircraft's navigation signals. Hence RCS reduction of hangars is essential.

(ii) Military stealth is another critical application of RCS reduction. The stealth aircrafts' and ships' RCS have to be reduced to prevent them from being attacked by the adversaries.

(iii) Reducing the RCS of antennas mounted in the aircraft and ship is an important application area. The antennas increase the RCS and thereby improve the visibility of the aeroplanes and ships used for stealth [17]. Therefore, it is essential to design the RCS reducing structures without affecting the radiating characteristics of the antenna.

3. CLASSIFICATION OF RCS REDUCTION TECHNIQUES

A broad classification of the different RCS reduction techniques is depicted in Figure 2. Scattering and absorption are the two fundamental techniques to reduce RCS, with the conventional methods being (i) shaping of the target and (ii) the use of RAM over the target. In recent times, metasurfaces have been widely researched for RCS reduction. Metasurfaces have the unique characteristic of being realizable both as scatterers and as absorbers. While metasurfaces are the primary focus, the conventional methods of shaping and RAM are briefly discussed in this section for completeness.

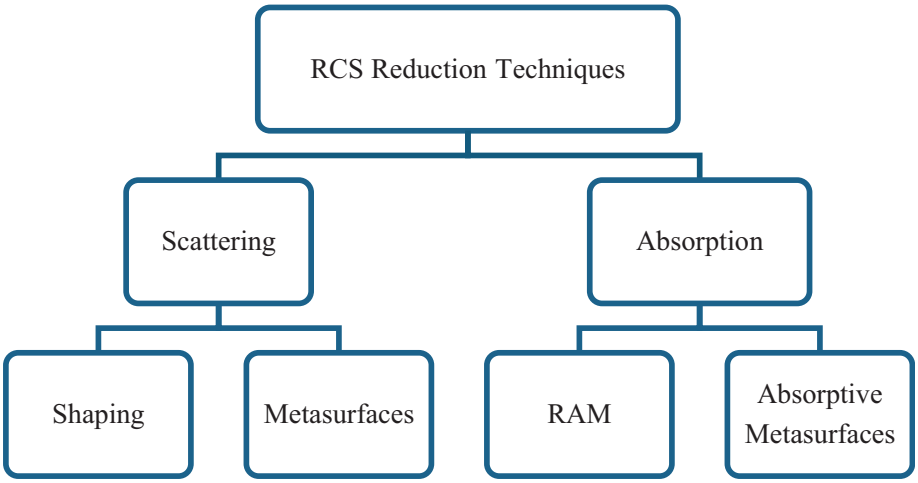

Figure 2. Classification of RCS reduction techniques.

3.1. Shaping

This type of RCS control is effective against most monostatic radars [18]. The two distinct ways of shaping explained in [19] to reduce the target RCS are (i) implementing a compact, smooth, blended external geometry and (ii) employing a faceted configuration to minimize reflections back to the illuminating radar. In [20], a low RCS value was obtained in the frontal aspect by maintaining a smooth curved shape. The Machan, an uncrewed aircraft developed in 1981, had reduced detectability owing to its diamond-shaped fuselage cross-section; the lower surface of the mainplane was flat to minimize glint. Optimization-based approaches to shape the target are discussed in [21] and [22].

The limitations of shape-based RCS reduction are that it is only effective for incident waves over a limited bandwidth [23] and over certain angles of incidence. Bandwidth can be improved using sophisticated gradient shapes. However, such intricate designs cannot be implemented for targets such as planes and ships due to aerodynamic and hydrodynamic requirements, which could affect the target's internal volume and stability [23].

3.2. Radar-Absorbing Materials (RAM)

RAM, another traditional method to reduce RCS, can be modelled based on one of the two functionalities [24]: (i) impedance matching and (ii) resonance.

3.2.1. Impedance-matched RAM

The three types of impedance-matching RAMs are pyramidal, tapered, and matched. In [25], wideband microwave pyramidal absorbers for a semi-anechoic chamber are presented, as shown in Figure 3(a). A tapered RAM uses a slab composed of a low-loss material mixed with a lossy material homogeneously dispersed parallel to the surface. These materials convert the incident radar energy into heat. The stealth aircraft Lockheed F-117 Nighthawk [26] uses a tapered RAM made of carbonyl iron balls suspended in epoxy resin to reduce its RCS. The matching layer absorber [27] places a transitional absorption layer between the incident and absorbing media, as shown in Figure 3(b). The thickness and impedances of the transition layer are between the two impedances that must be matched. This matching occurs when the thickness of the matching layer is one-quarter of the wavelength of the radiation in the layer, which makes them narrowband absorbers.

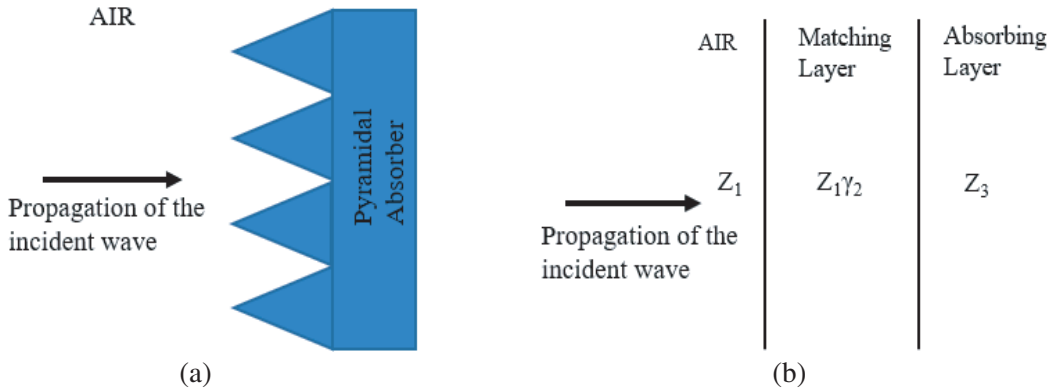

Figure 3. (a) Pyramidal absorbers and (b) matched layer absorbers redrawn based on [24].

3.2.2. Resonant RAM

Resonant RAM is also known as a tuned or quarter wavelength absorber. Here, the impedance is not matched between the incident and absorbing media. The configuration results in reflection and transmission at the first interface. The reflected wave at the first interface experiences a phase shift of π, while the transmitted electromagnetic wave travels through the absorbing medium and is reflected from the metal backing. This second reflection results in a phase reversal of π and the distance travelled introduces a phase of π before the wave propagates back to the incident medium. This results in destructive interference between the two reflected waves, thereby resulting in reduced RCS. Salisbury screen absorbers [28] and Jaumann absorbers [29] are the two types of resonant RAM and are depicted in Figures 4(a) and 4(b). Though RAMs are reasonably effective, they are usually thick, expensive, and provide RCS reduction only over a narrow bandwidth. Bandwidth enhancement is achieved by increasing the bulkiness of the structure, making it less suitable for practical implementation.

A metasurface-based approach appears to be a more effective alternative to the traditional RCS reduction methods. The rest of the paper discusses the different kinds of metasurfaces used for RCS reduction.

4. RCS REDUCTION BASED ON SCATTERING METASURFACES

Metasurfaces are periodic structures using unit cell elements that are designed to vary the reflection magnitudes and phases of the incident wave. Positioning these unit cells or microcells in different

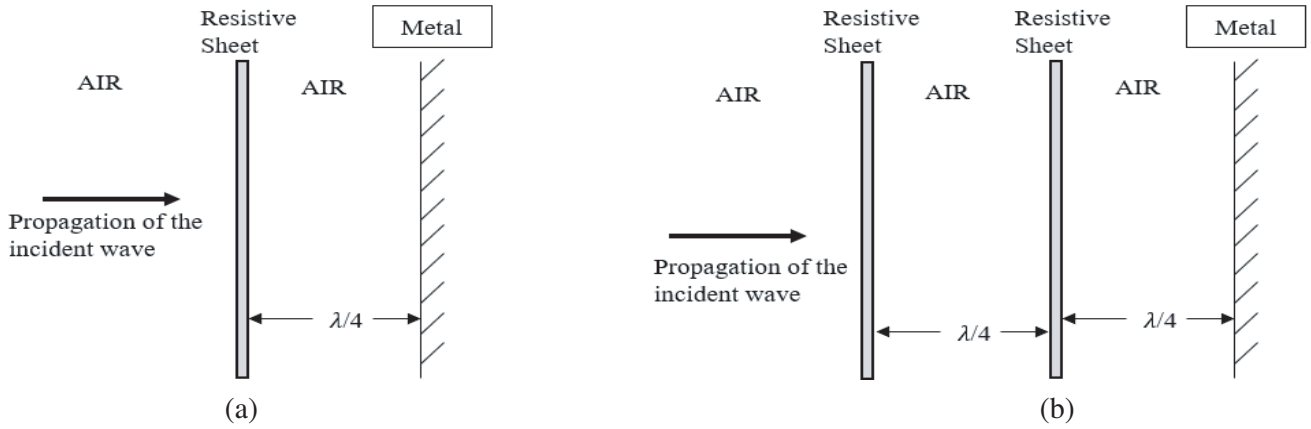

Figure 4. (a) Salisbury screen absorber and (b) Jaumann absorber redrawn based on [24].

configurations or patterns generates macrocells or tiles. An array of these macrocells or tiles, arranged in various ways, comprise the metasurface. The metasurface function depends on the element geometry, arrangement of the unit cells and, in turn, the tile positioning. Based on the functional operation of the metasurface, this paper classifies metasurfaces as (i) phase gradient metasurfaces (PGMS), (ii) checkerboard metasurfaces (CMS), (iii) polarization conversion metasurfaces (PCMS), (iv) coding-based metasurfaces (COM), (v) reconfigurable metasurfaces (RMS), and (vi) time-varying metasurfaces. The first four are passive methods, while the last two are active ways of reducing RCS.

All the different forms of metasurface share the common concept of manipulating the wavefront, which can be explained using Huygens' metasurface and bianisotropic metasurfaces. The Huygens' metasurface synthesizes impedance and admittance surfaces in order to refract or reflect an incident plane wave at certain angles. This is discussed in [30, 31], and [32]. This method can be used to design any of the different types of metasurface for RCS reduction applications. A synthesis procedure to design omega-bianisotropic metasurfaces (O-BMSs) was reported in [33] that uses the auxiliary modes guided between the PEC and the O-BMS to obtain the surface parameters. The surfaces thus synthesized reflect the incident plane waves in a desirable direction which can be used for RCS reduction. Polarization conversion-based metasurfaces can also be synthesized using the procedure reported for Huygens' metasurface and bianisotropic metasurfaces [34, 35]. From [28–33], it is observed that Huygens' metasurface and bianisotropic metasurfaces can be realized in any of the forms of metasurface classified above for RCS reduction.

In what follows, each of the metasurface types is discussed in detail. The discussion covers working mechanisms and advances in the field of RCS reduction.

4.1. Phase Gradient (Graded Index) Metasurfaces

The PGMS for RCS reduction works on the principle of anomalous reflection and conversion of propagating wave to surface wave. This section first discusses the working mechanism of PGMS based on the generalized Snell's law and then reviews the different metasurfaces reported for RCS reduction.

Although the basic concept behind the functioning of PGMS can be traced to diffraction gratings, it became well known only after the proposal of the generalized Snell's law in [36]. According to the generalized Snell's law, a surface with phase discontinuity deflects the signal away from the specular direction as per the following expression:

$$\sin(\theta_t)\, n_t - \sin(\theta_i)\, n_i = \frac{\lambda_0}{2\pi}\frac{d\varphi}{dx} \tag{1}$$

where n_t and n_i are the refractive indices of the two media; λ_0 is the free-space wavelength; $d\varphi$ is the phase difference between the adjacent cells; and dx is the spacing between the elements. A pictorial representation of the generalized Snell's law is shown in Figure 5. A vital design feature of a PGMS is that the elements used to design it should only span the 2π phase range based on expression (1).

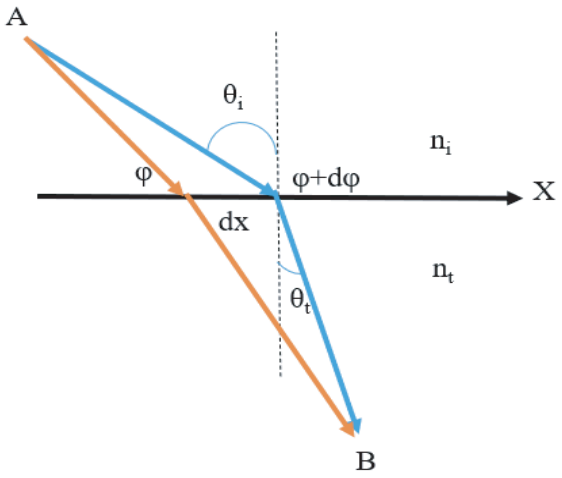

Figure 5. Schematic to derive the generalized Snell's law of refraction, redrawn based on [36].

This concept was practically demonstrated using v-shaped nanoantennas [36]. The basic building block of these PGMSs is the element that alters the reflection phase and magnitude of the incident wave. Elements with varying phases are arranged in a gradient fashion to form a tile; these tiles are repeated to obtain the phase gradient metasurface. When the elements used to construct the metasurface are designed to span the 2π phase range over a wide bandwidth, wideband RCS reduction is attained. The challenge of creating broadband elements is the dependency of the size of the unit cell to that of the operating frequency range.

Graded index structures reduce the specular reflection in two ways: (i) anomalous reflection [37], and (ii) converting the propagating wave (PW) into surface waves (SW) [38]. Using low-Q metasurfaces, [39] reported a 40% reduction in RCS bandwidth. Split-ring-based PGMS, as explained in [40], reduces the RCS by using both surface wave conversion and anomalous reflection. This feature has resulted in a bandwidth enhancement of up to 74%.

The working mechanism is discussed as follows.

Let k_i be the wavenumber of the incident signal and k_r be the wavenumber of the reflected signal. The phase deviation along the x and y axes are $\nabla\phi_x$ and $\nabla\phi_y$, respectively, while k_{ix} and k_{iy} represent the x and y components of the incident wave vector. The two cases occur under the following conditions:

(i) $k_r > k_i$, the reflected waves lie along the PGMS plane, as shown in Figure 6(a). The in-plane direction of the coupled surface waves is

$$\varphi = \arctan\left(\frac{K_{iy} + \nabla\phi_y}{K_{ix} + \nabla\phi_x}\right) \tag{2}$$

(ii) $k_r < k_i$, anomalous reflection occurs as shown in Figure 6(b). The reflected angle is

$$\theta_r = \arcsin\left(\frac{\sqrt{(\nabla\phi_x + k_{ix})^2 + (\nabla\phi_y + k_{iy})^2}}{k_i}\right) \tag{3a}$$

$$\varphi_r = \arctan\left(\frac{K_{iy} + \nabla\phi_y}{K_{ix} + \nabla\phi_x}\right) \tag{3b}$$

Researchers later reported a variety of elements featuring a wide bandwidth configured in a gradient fashion. In addition to wide bandwidth, a 25° wide-angle response was reported in [41] using a windmill-shaped element. An ultra-thin hybrid PGMS was reported in [42], reducing the RCS in two frequency bands at 8.7 GHz and 11.4 GHz. A wideband and a wide-angle RCS reduction PGMS was reported in [43], where the phase gradient was based on the Pancharatnam-Berry phase and used a circularly polarized illuminating wave. A cost-effective metasurface presented in [44] considered both the reflection

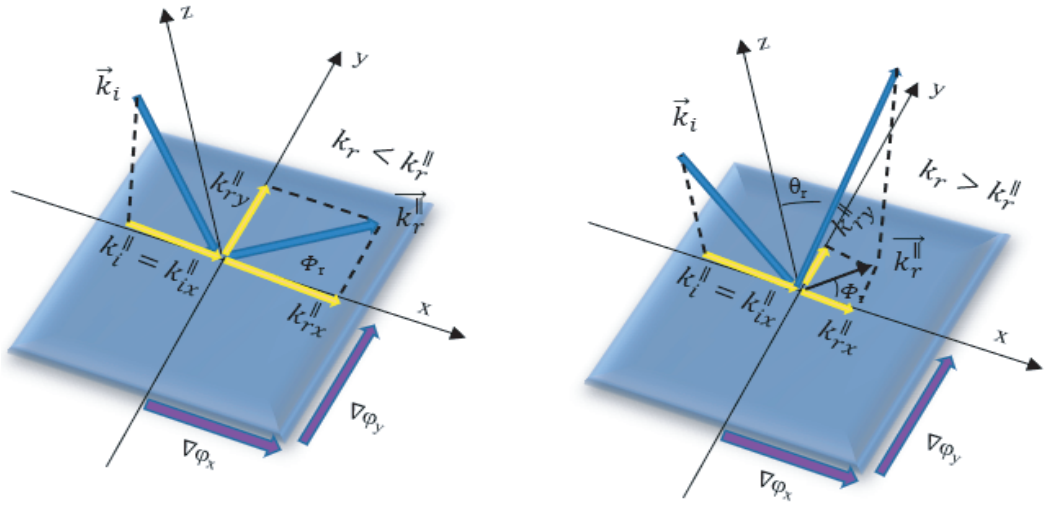

(a) (b)

Figure 6. Two anomalous effects of 2D reflective PGMS illuminated by electromagnetic waves: (a) surface-wave coupling and (b) anomalous reflection redrawn based on [40].

amplitude and phase in the design, resulting in a much wider bandwidth of 128% and a wide-angle of up to 60°.

All the above-discussed works reduce the RCS of flat metal targets, whereas it is also used to reduce the RCS of antennas. RCS reduction of a slot array antenna using PGMS was reported in [45]. The antenna's operating frequency band was 4.1–4.26 GHz, while the RCS reduction was observed over the frequency range of 7–16.8 GHz. This configuration is called out-of-band because the RCS reduction and antenna operation are in two different bands. The PGMS reported in [45] is shown in Figure 7.

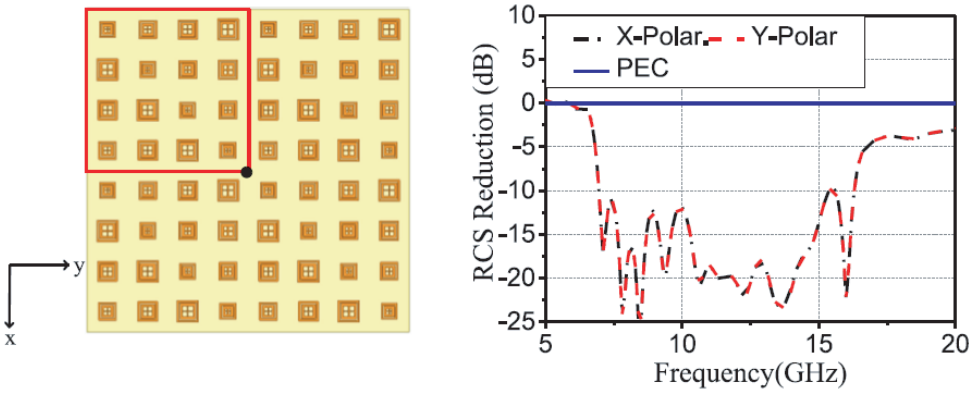

(a) (b)

Figure 7. PGMS. (a) Geometry of the 2D PGMS, and (b) normalized monostatic RCS reduction with respect to a perfect electric conductor plate [45]. Reproduced with permission.

The techniques to improve bandwidth using PGMS can be consolidated as, i) suitable element selection that spans the phase range of 2π over a wide band, (ii) element design that constitutes both anomalous reflection and PW to SW conversion, and (ii) amplitude and phase gradient surfaces. A consolidated summary of the features of PGMS is listed in Table 1.

Table 1. Summary of features — PGMS.

SI. No.	Ref. No.	Year	Working mechanism	a) Monostatic/bistatic b) RCS reduction frequency range (fractional bandwidth) c) Angular range if reported		Array size	Unit cell size
				Simulated	Measured		
1	[38]	2012	PW to SW conversion	a) Monostatic b) 15 GHz	a) Monostatic b) 15 GHz	–	$0.125\lambda_0 \times 0.3\lambda_0$
2	[39]	2013	Anomalous reflection	a) Monostatic b) 8 GHz–11 GHz (40%)	a) Monostatic b) 8–11 GHz (40%)	–	$0.16\lambda_0 \times 0.23\lambda_0$
3	[40]	2014	PW to SW conversion & anomalous reflection	a) Monostatic b) 8 GHz and 12.4 GHz	a) Monostatic b) 8 GHz and 12.4 GHz	–	$0.20\lambda_0 \times 0.20\lambda_0$
4	[41]	2014	Anomalous reflection	a) Monostatic/bistatic b) 8 GHz to 13 GHz (48%)	a) Monostatic/bistatic b) 8 GHz to 13 GHz (48%)	$10.5\lambda_0 \times 10.5\lambda_0$	$0.20\lambda_0 \times 0.20\lambda_0$
5	[42]	2017	Anomalous reflection	a) Monostatic b) 8.9 GHz and 11.4 GHz	a) Monostatic b) 8.9 GHz and 11.4 GHz	$10.4\lambda_0 \times 10.4\lambda_0$	$0.20\lambda_0 \times 0.20\lambda_0$
6	[43]	2017	Anomalous reflection	a) Monostatic b) 9.85 GHz–19.37 GHz (65%)	a) Monostatic b) 9.85 GHz–19.37 GHz (65%)	$8.25\lambda_0 \times 8.25\lambda_0$	$0.25\lambda_0 \times 0.25\lambda_0$
7	[45]	2018	Anomalous reflection	a) Monostatic b) 7 GHz to 16 GHz (78%)	–	$5.7\lambda_0 \times 5.7\lambda_0$	$0.69\lambda_0 \times 0.69\lambda_0$
8	[44]	2020	Anomalous reflection	a) Monostatic/bistatic b) 9 GHz to 40.7 GHz (128%)	a) Monostatic/bistatic b) 9 GHz to 40.7 GHz (128%)	$19\lambda_0 \times 19\lambda_0$	$0.75\lambda_0 \times 0.75\lambda_0$

4.2. Checkerboard Metasurfaces

CMS is another type of metasurface to reduce the RCS that works on the principle of destructive interference. As the name implies, CMS is constructed using a pair of subarrays that alternate in a checkerboard-like fashion. Each subarray is made of a periodic arrangement of unit cells. The reflection phases of the two-unit cells are designed to provide 0° and 180°, respectively. Hence, the reflected signals cancel out in the far-field. This phenomenon is explained using two sinusoidal signals in Figure 8. Appropriate design of the unit cells results in enhanced bandwidth.

It appears that the first checkerboard-based idea for RCS reduction was reported in [47]. This paper presents a checkerboard arrangement of an artificial magnetic conductor (AMC) and a perfect electric conductor (PEC). The AMC and PEC reflect signals with 0° and 180° phases, respectively, causing the cancellation of the fields in the far-field and resulting in RCS reduction. However, the effective bandwidth remained narrow. In [48], the authors examined an AMC-PEC pair with an AMC-AMC pair and reported that the AMC-AMC-based CMS provided a wider bandwidth than that of the AMC-PEC pair. Subsequently, researchers have enhanced the RCS reduction bandwidth by using a suitable combination of elements. A 32% bandwidth was reported in [49] by maintaining a $180 \pm 30°$ phase difference between two AMCs. Theoretical prediction of the grating lobe direction is explained in [50] using a Jerusalem cross-based checkerboard configuration, which offers a fractional bandwidth of 40%. The 10 dB RCS reduction bandwidth reported had a spike of 8 dB, which was attributed to

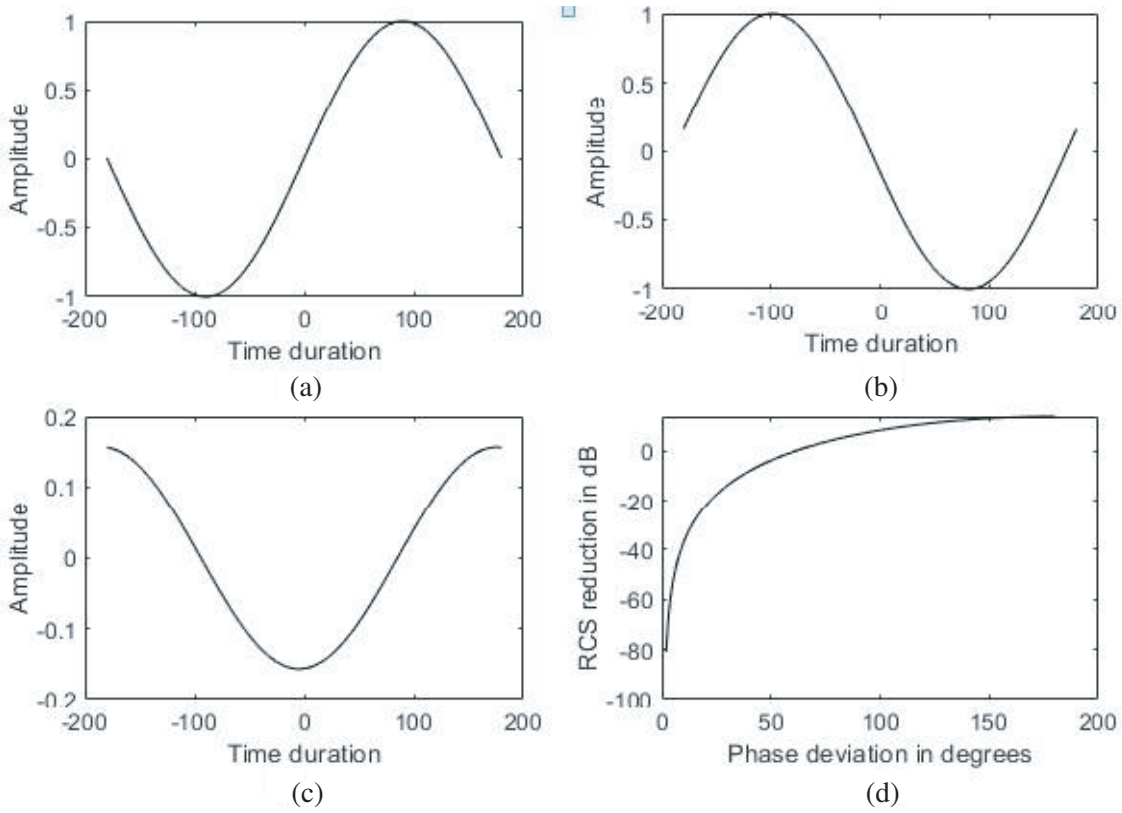

Figure 8. Demonstration of destructive interference: (a) sinusoidal signal, $s(t)$, (b) signal phase shifted, $s(t+180+10)$, (c) $s(t)+s(t+180+10)$, (d) phase deviation vs RCS reduction [46]. Reproduced with permission.

the finite size of the array. In [51], an empirical expression (4) for RCS reduction in terms of the unit cell's reflection coefficient and phase was reported. It was also stated that a $180 \pm 37°$ phase deviation between unit cells is required for an RCS reduction of 10 dB.

$$RCS\,reduction = \left| \frac{A_1 e^{j\varphi_1} + A_2 e^{j\varphi_2}}{2} \right| \tag{4}$$

where (A_1, φ_1) and (A_2, φ_2) are the amplitudes and phases of unit cells 1 and 2, respectively.

RCS reduction over a dual-band was presented using two dual-resonance unit cells in [52]. Blended CMSs were reported in [53] using single- and dual-resonance AMCs, offering a bandwidth of 83%. Further, they present an enhancement in the bandwidth of up to 91% by using four AMCs while stretching the phase deviation beyond $180 \pm 37°$ for two of the AMCs. A bandwidth of 91.5% was reported in [54], where dual- and triple-resonance AMCs were used. Additionally, the cancellation condition of the checkerboard structure was analytically derived using the equivalent transmission line model. In [55], the bandwidth was improved from 60% to 65% by using simple arcs at the corners, aiding in surface wave suppression, as shown in Figure 9.

The CMSs discussed so far were designed by the appropriate choice of two unit cells and are planar structures. However, a very wide bandwidth ratio of 5.87 : 1 was obtained in [56] using a multi-element non-planar CMS, where RCS was reduced due to scattering cancellation of the multiple elements. A triple-layered checkerboard structure reported in [57] provided a bandwidth of 96%.

A unified theory to explain phase-gradient and checkerboard configuration is presented in [58]. It combines the concepts of Snell's law and array theory and also discusses a synthesis procedure using Schelkenoff's polynomial method and the phasor diagram method. A semi-empirical expression for determining the RCS reduction in terms of the unit cell's reflection magnitude and phase is mentioned

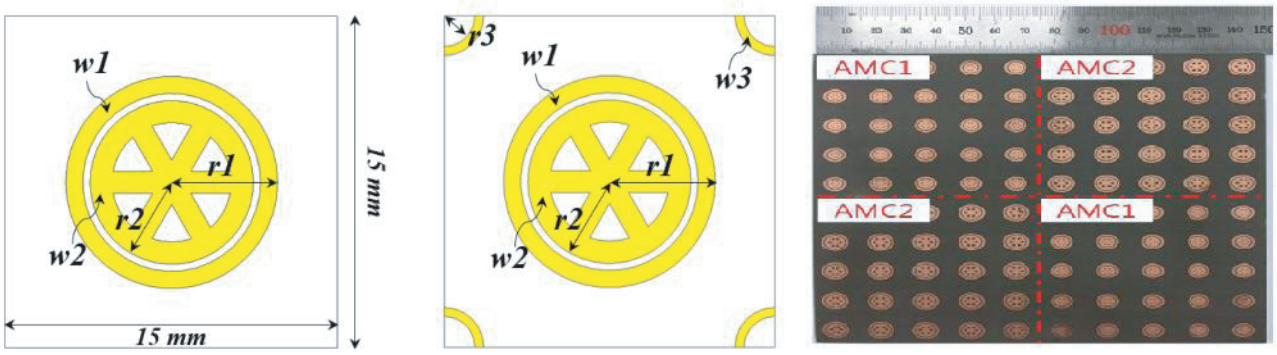

(a) (b) (c)

Figure 9. CMS reported in [55]: (a) unit cell 1, (b) unit cell 2, and (c) CMS constructed using (a) and (b). Reproduced with permission.

below.

$$RCS\ Reduction = \left| \frac{\sum_{p=1}^{N} \sqrt{\sigma_{3-D_p}} e^{j(p-1)\psi}}{\sqrt{\sigma_{3-D_{ref}}}} \right| \tag{5}$$

where σ_{3-D_p} is the echo area of the unit cells, and ψ is the phase shift between adjacent cells.

An optimization procedure linking the simulation tool CST and MATLAB reported in [46] further enhanced the bandwidth of known broadband structures. This study also reported a much wider 15 dB RCS reduction bandwidth of 48%. Most of the above-discussed work uses a Rogers substrate, whereas [59] presented a low-cost CMS on an FR4 substrate and proposed a modified phase deviation criteria for wide bandwidth.

All the above-CMSs were used to reduce the RCS of a flat metal target, while [60] reports CMSs designed for the RCS reduction of dihedral corners. In [61], the CMS was used for the RCS reduction of curved targets.

The bandwidth has been comprehensively enhanced in two ways: (i) appropriate choice of elements and (ii) surface wave suppression. A summary of the essential features is provided in Table 2.

4.3. Polarization Conversion Metasurfaces

The PCMS, which works on polarization conversion, is the next type of RCS reduction metasurface. Element design is essential for constructing a PCMS since it converts the polarization of an incident wave to its orthogonal state upon reflection. This conversion by the PCMS results in the radar being unable to detect the reflected signal, resulting in RCS reduction. The RCS reduction level depends on the polarization conversion efficiency of the metasurface. The elements used to explain the concept of polarization conversion are shown in Figure 10. The polarization conversion mechanism is explained with reference to [62]. Figure 10 depicts the incident and reflected fields.

The elements generate symmetric and antisymmetric modes via electric field components along the v- and u-axes, respectively. When a linearly polarized plane wave is incident along the x-direction, E_i can be decomposed into parallel and perpendicular components E_{iv} and E_{iu}, respectively. The function along the 'v' direction is considered as a PEC due to the electric resonance; therefore, after being reflected, E_{rv} and E_{iv} are out of phase, as shown in Figure 11(a). The function in the 'u' direction is considered a high-impedance surface because of its magnetic resonance; hence, E_{ru} and E_{iu} are in phase. The resultant of E_{rv} and E_{ru} is the y-polarized reflected wave 'E_r' obtained by converting the illuminating x-polarized wave 'E_i'. Element 1 in Figure 11(b) behaves in the opposite way. The reflected wave mainly constitutes the cross- and co-polarized components R_{xy} and R_{yy}, which can be computed

Table 2. CMS — Summary of features.

SI. No.	Ref. No.	Year	a) Monostatic/bistatic b) Simulated RCS reduction frequency range (fractional bandwidth) c) Angular range if reported		Array size	Unit cell size
			Simulated	Measured		
1	[47]	2007	a) Monostatic/bistatic b) 15.32 GHz	a) Monostatic/bistatic b) 15.32 GHz	$22\lambda_0 \times 14\lambda_0$	$1\lambda_0 \times 1\lambda_0$
2	[48]	2010	a) Monostatic b) 5.78 GHz	a) Monostatic b) 5.78 GHz	$3.5\lambda_0 \times 3.5\lambda_0$	$0.18\lambda_0 \times 0.18\lambda_0$
3	[50]	2013	a) Monostatic/bistatic b) 14.4–28.8 GHz (40.88%)	a) Monostatic/bistatic 14.8 to 22.7 GHz (42%)	$20.7\lambda_0 \times 13.8\lambda_0$	$0.25\lambda_0 \times 0.25\lambda_0$
4	[51]	2015	a) Monostatic/bistatic b) 4.10–7.59 GHz (63%)	a) Monostatic b) 3.8–8.8 GHz (60%)	$4.68\lambda_0 \times 4.68\lambda_0$	$0.29\lambda_0 \times 0.29\lambda_0$
5	[52]	2016	a) Monostatic b) 3.94–7.40 GHz (61%) 8.41–10.72 GHz (24%)	a) Monostatic b) 3.94–7.40 GHz (61%) 8.41–10.72 GHz (24%)	$2.1\lambda_0 \times 2.1\lambda_0$	$0.34\lambda_0 \times 0.34\lambda_0$
6	[53]	2017	a) Monostatic/bistatic b) 3.75–10 GHz (91%)	a) Monostatic b) 3.75–10 GHz (91%)	$2.6\lambda_0 \times 2.6\lambda_0$	$0.32\lambda_0 \times 0.32\lambda_0$
7	[54]	2019	a) Monostatic/bistatic b) 3.78–10.08 GHz (90.9%)	a) Monostatic b) 3.77–10.14 GHz (91.5%)	$2.98\lambda_0 \times 2.98\lambda_0$	$0.37\lambda_0 \times 0.37\lambda_0$
8	[55]	2019	a) Monostatic/bistatic b) 8–16 GHz (67.8%)	a) Monostatic b) 7.98–16.32 GHz (68.6%)	$6\lambda_0 \times 6\lambda_0$	$0.6\lambda_0 \times 0.6\lambda_0$
9	[46]	2021	a) Monostatic/bistatic b) 4.8–14.8 GHz (102%)	Monostatic b) 4.89–14.3 GHz (98%)	$7.8\lambda_0 \times 7.8\lambda_0$	$0.49\lambda_0 \times 0.49\lambda_0$
10	[59]	2021	a) Monostatic b) 4.3–12.6 GHz (98%)	a) Monostatic b) 4.1–12.3 GHz (100%)	$6.56\lambda_0 \times 6.56\lambda_0$	$0.41\lambda_0 \times 0.41\lambda_0$
11	[56]	2018*	a) Monostatic/bistatic b)5.5 to 32.3 GHz (141%)	a) Monostatic b) 5.5 to 32.3 GHz (141%)	$14\lambda_0 \times 14\lambda_0$	$0.5\lambda_0 \times 0.5\lambda_0$

*non-planar structure

using the following expressions from [62].

$$R_{xy} = \frac{|E_{rx}|}{|E_{iy}|} = \sqrt{\frac{(1 - \cos\Delta\varphi)}{2}} \tag{6}$$

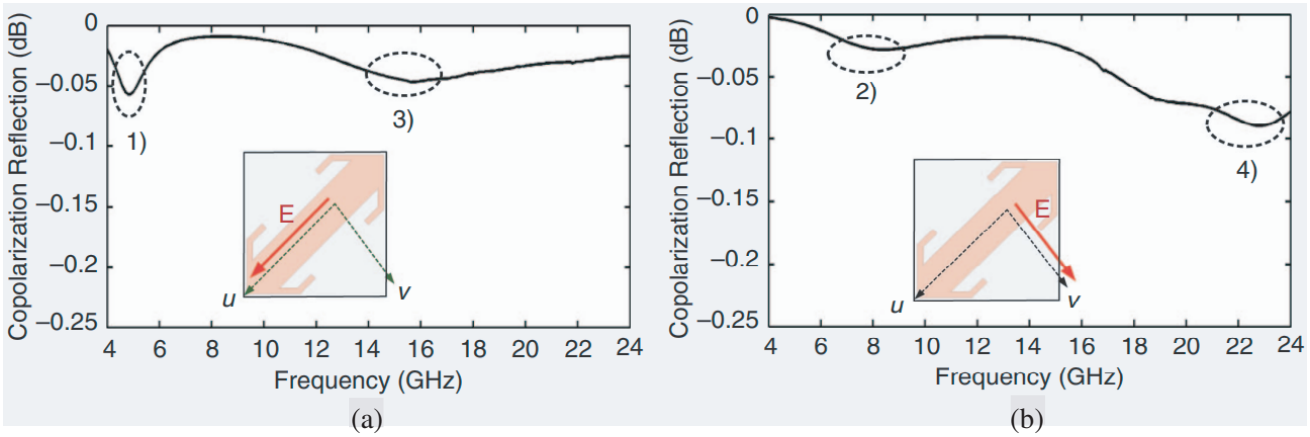

Figure 10. Four resonances of the unit cell: (a) U polarized case, and (b) V polarized case [62]. Reproduced with permission.

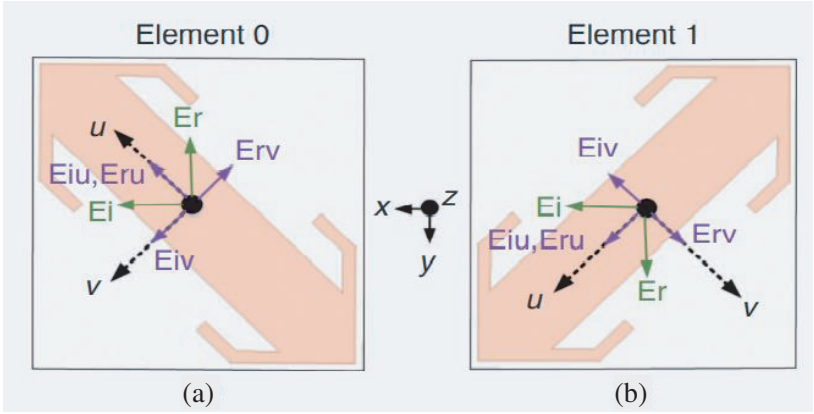

Figure 11. An intuitive image of the x-polarized wave incident in the unit cells. (a) Element 0, and (b) Element 1 [62]. Reproduced with permission.

$$R_{yy} = \frac{|E_{ry}|}{|E_{iy}|} = \sqrt{\frac{(1+\cos\Delta\varphi)}{2}} \tag{7}$$

where $\Delta\varphi$ is defined as the phase difference between R_{xy} and R_{yy}, and the polarization conversion ratio (PCR) is defined as in Eq. (8) from [62]:

$$PCR = \frac{R_{xy}^2}{R_{xy}^2 + R_{yy}^2} \tag{8}$$

A double-headed arrow element employed in the polarization conversion metasurface reported in [63] provided 100% polarization conversion at four frequencies, resulting in a 10 dB RCS decrease at these four frequency points. At the same time, a 3 dB reduction in RCS was observed over the frequency range of 6.6–23.9 GHz. The metasurface reported in [64] used an oblique split-ring resonator and a cut-wire resonator, enhancing the 10 dB RCS reduction bandwidth to 60% with 100% PCR over the bandwidth 9.4–19.2 GHz. Ultra-wideband polarization rotation reflective surfaces (PRRS) constructed using a periodic array of quasi-L-shaped patches, reported in [65], offers a polarization rotation bandwidth of 103%, and PCR is greater than 50%. The metasurface structure reported in [66] offered a 10 dB RCS reduction over the frequency range 17–42 GHz. It also offered a wide-angle of up to 50° by combining

the use of a checkerboard metasurface with rotated unit cells. The element reported in [67] consisted of a square and L-shaped metallic patches printed on a grounded dielectric substrate. The two patches were connected to the ground by two metallic vias loaded in a diagonal direction. A superstrate covered the dual-patch unit cell, and the 10 dB RCS reduction bandwidth was about 98%. The polarization conversion metasurface explained in [68] consisted of a double-headed arrow unit cell with 90°, 180°, and 270° rotations to create destructive interference. It provided an ultra-wideband 10 dB RCS reduction from 9–40 GHz (126.5%) for TM- and TE-polarized incident waves.

The PCMSs reported in [69–72] provide enhanced bandwidth through a suitable choice of elements, where the unit cells are a variation of the diagonally represented arrow structure. The discussion so far was on RCS reduction of flat metal targets; the RCS reduction of antennas using PCMS is discussed next.

RCS reduction of antennas using PCMS is reported in [73–77]. In [73], PCMS along with a partially reflecting surface (PRS) enhances the antenna's gain and reduces the antenna's RCS. The PCM and PRS are printed on two sides of a substrate above the microstrip patch antenna to form a Fabry-Perot resonant cavity. Due to the symmetrical arrangement of the PCMS unit and its mirror unit, very high wideband radar cross-section reduction was obtained in both x- and y-polarizations. Wideband RCS reduction ranging from 9–20 GHz with a maximum in-band value of 20 dB at 9.4 GHz, and an out-of-band value of 33 dB was reported. A 2.5-dimensional PCMS was reported in [74], which offered a high PCR over an ultra-wideband whose fractional bandwidth is 99.5% for the x and y-polarized incident waves with a PCR of 96%.

In summary, most of the PCMS elements are variations of the slanted arrow-shaped elements that result in polarization conversion. A comparison of the performance metrics of PCMSs is presented in Table 3.

Table 3. PCMS — Summary of features.

SI. No.	Ref. No.	Year	a) Monostatic/bistatic b) RCS reduction frequency range (fractional bandwidth) c) Angular range if reported		Array size	
			Simulated	Measured		Unit cell size
1	[63]	2014	a) Monostatic b) 6.8 GHz, 12.17 GHz, 15.45 GHz, and 23.13 GHz	a) Monostatic b) 6.8 GHz, 12.17 GHz, 15.45 GHz, and 23.13 GHz	$20\lambda_0 \times 20\lambda_0$	$0.30\lambda_0 \times 30\lambda_0$
2	[65]	2016	a) Monostatic b) 10.74–17.2 GHz	a) Monostatic b) 10.74–17.2 GHz	$22\lambda_0 \times 14\lambda_0$	$0.28\lambda_0 \times 28\lambda_0$
3	[64]	2016	a) Monostatic b) 10.2 to 19.3 GHz	a) Monostatic b) 10.2 to 19.3 GHz	$3.4\lambda_0 \times 3.4\lambda_0$	$0.29\lambda_0 \times 29\lambda_0$
4	[66]	2016	a) Monostatic/bistatic b) 17 GHz–42 GHz c) 10–50 degrees	a) Monostatic b) 17 GHz–42 GHz	$21\lambda_0 \times 21\lambda_0$	$0.30\lambda_0 \times 30\lambda_0$
5	[68]	2019	a) Monostatic/bistatic b) 14.5 to 41 GHz	a) Monostatic/bistatic b) 16.8 to 37.3 (126.5%)	$16\lambda_0 \times 16\lambda_0$	$0.59\lambda_0 \times 59\lambda_0$
6	[72]	2021	a) Monostatic/bistatic b) 9.5–13.9 GHz (32%) /15.2–20.4 GHz (30%) c) 45 degrees	a) Monostatic/bistatic b) 10.2–14.0 GHz (32%) /15.3–20.7 GHz (30%) C) 45 degrees	$12\lambda_0 \times 12\lambda_0$	$0.5\lambda_0 \times 5\lambda_0$

4.4. Coding Metasurfaces

Digital metamaterials were first introduced in [78], which considered unit cells used in the construction of the metasurface as binary digits. Coding, digital, and programmable metasurfaces were reported in [79], where the same metasurface was used for multiple functionalities, including RCS reduction. The unit cells used to realize the metasurface offering a phase response of 0° and 180° are assigned the digits 0 and 1 and are called binary coding metasurfaces. In a similar way, 2-bit coding metasurfaces use four elements with phases 0°, 90°, 180°, and 270°. N-bit coding metasurfaces use $2\pi/N$ elements. The far-field pattern of any coding metasurface can be determined using the expression (9), from which the directivity is estimated and is then used to estimate the RCS reduction.

$$f(\theta,\varphi) = f_e(\theta\varphi)\sum_{m=1}^{N}\sum_{n=1}^{N}\exp\left[-i\left\{\varphi(m,n)+kD\sin\theta\left[(m-1/2)\cos\varphi+(n-1/2)\sin\varphi\right]\right\}\right] \tag{9}$$

$$RCS\,reduction = \frac{\lambda^2}{4\pi N^2 D^2}\left[Dir(\theta,\varphi)\right] \tag{10}$$

where θ and φ are the elevation and azimuthal angles, respectively; k is the wavenumber; D is the spacing between the elements; N is the total number of elements in the array; (m,n) is the position of the elements; and $\varphi(m,n)$ refers to the reflection phase of the individual elements at position (m,n).

Checkerboard metasurfaces are considered 2-bit coded metasurfaces, while phase gradient metasurfaces are multi-bit coded metasurfaces. [80, 81], and [82] reported the reflection and scattering of THz waves in an anomalous manner by using coding metamaterials. One-bit coding materials are reported in [80], while [81] reported 1-bit coding, 2-bit coding, and multi-bit coding metasurfaces using Minkowski closed-loop elements designed at terahertz frequencies.

The coding phase gradient metasurface reported in [43] considers the phase gradient elements as the coding bits. It utilizes the N-shaped element as the unit cell, with a co-polarization reflection characteristic under circularly polarized incident waves. The coding features for 1-, 2-, and multi-bit are designed based on the Pancharatnam-Berry phase. The expressions (11) and (12) provide the reflected wave direction based on the angle at which the incidence occurs, and the phase variation occurs along the x and y directions:

$$\theta_a = \sin^{-1}\left(\frac{\sqrt{\left(k_0\sin\theta_i\cos\varphi_i+\nabla\varphi_x\right)^2+\left(k_0\sin\theta_i\cos\varphi_i+\nabla\varphi_y\right)^2}}{k_0}\right) \tag{11}$$

$$\varphi_a = \tan^{-1}\left(\frac{k_0\sin\theta_i\cos\varphi_i+\nabla\varphi_y}{k_0\sin\theta_i\cos\varphi_i+\nabla\varphi_x}\right) \tag{12}$$

where θ_a and φ_a are the elevation and azimuth angles of the main lobe for the primary pattern, and $\nabla\varphi_x = d\varphi_x/dx$ and $\nabla\varphi_y = d\varphi_y/dy$ are the phase gradients along the x- and y-directions, respectively, where $d\varphi_x$ and $d\varphi_y$ are the phase differences between adjacent unit cells in the x-direction and y-direction, and dx and dy are the length and width of the unit cell, respectively.

Bandwidth enhancement has been reported in [83–85, 62] by means of an optimization-based design of coded metasurfaces. A coding metasurface and bandpass frequency selective surface were combined in [83] to simultaneously achieve high-efficiency transmission and broadband RCS reduction. The functional performance of both transmission and RCS reduction was attained by designing the metasurface based on the particle swarm optimization algorithm. This led to a 15 dB RCS reduction over the frequency range of 8.5–13.5 GHz. In [84], a 4-bit reflective coding metasurface with a polarization-insensitive unit cell was designed for wideband radar cross-section reduction using the discrete water cycle algorithm. The 4-bit unit cells are represented in Figure 12. A wideband metasurface offering 125% RCS reduction based on polarization conversion and binary coding was reported in [62], in which the group search algorithm was used. A 3-bit random coding PCM comprising eight elements reduced RCS over the frequency range 18.3–42.2 GHz [85].

A coding diffused metasurface reported in [86] used an array factor and ergodic algorithm to design the AMC blocks, which in turn were used to construct the 2D array. This has been reported to be a faster design approach and offers a bandwidth of 27.8%. Another diffused coding metasurface with a

Phase and shape / Multi-bit	0°	22.5°	45°	67.5°	90°	112.5°	135°	157.5°	180°	202.5°	225°	247.5°	270°,	292.5°	315°	337.5°
1-bit	0								1							
2-bit	00				01				10				11			
3-bit	000		001		010		011		100		101		110		111	
4-bit	0000	0001	0010	0011	0100	0101	0110	0111	1000	1001	1010	1011	1100	1101	1110	1111

Figure 12. 1-, 2-, 3- and 4-bit coding metasurfaces using different sizes of unit cells, reproduced from [84].

spiral track arrangement, reported in [87], has offered improvement in bandwidth up to 69%. A matrix-type coding metasurface further enhanced the bandwidth to 87% in [88]. In [89], a one-bit coding diffusion metasurface is reported to provide wider bandwidth compared to a CMS.

A non-planar coded diffusive metasurface [90] offered 129% fractional bandwidth over the frequency range 6.4–30.1 GHz. It is observed that non-planar structures, in general, provide wider bandwidth.

All the above-mentioned metasurfaces were used to reduce the RCS of a flat metal target. By contrast, [91] reports the RCS reduction of a cylindrical metal target utilizing a flexible indium-tin-oxide-based ultrathin coding metasurface (less than 0.1 wavelengths thick) with high optical transparency. A phase-quantized coded metasurface was reported in [92], and [93] reports edge backscattering suppression using coded metasurfaces.

To summarize, coded metasurfaces can be constructed using any of the three metasurfaces CMS, PGMS, or PCMS, or a combination of them. When these designs are made using an optimization procedure, further enhancement in the RCS reduction bandwidth is obtained.

A summary of the essential features of the coding based metasurface is provided in Table 4 below.

4.5. Reconfigurable Metasurfaces

Passive metasurfaces have the drawback of being operated only at particular fixed frequency bands. If the frequency has to be altered, then the unit cell must be redesigned. This limitation has been overcome by designing metasurfaces that can be tuned with external triggering circuits. Due to this tuning feature of the metasurface, dynamic functionality is integrated into the design.

The metasurface's tunability can be either integrated over the whole metasurface or at the unit cell level. Metasurfaces designed on stimuli-responsive materials change their physical properties in response to external conditions, such as temperature, pressure, humidity, electric/magnetic fields, and light. As a result, the functionality of the metasurface is changed as a whole. Hence, this type of metasurface is referred to as a globally tuned metasurface. Owing to the practical difficulties of changing the pressure and humidity, researchers have focused on tuning parameters such as the electric field, magnetic field, light, and temperature. Graphene and liquid crystals are used to design globally tuned metasurfaces. When the functional performance of the metasurface is altered at the unit cell level, it is called a locally tuned metasurface. PIN diodes, varactor diodes, and lumped components are used in tuning the individual unit cells.

4.5.1. Globally Tuned

Globally tuned metasurfaces are reported in [94–96]. [94] describes the actively tunable terahertz wave coding metasurfaces using a vanadium-embedded metallic patch. The coding scheme is altered using the metal-insulator transition of vanadium dioxide (VO_2) at approximately 68°C, which aids in RCS reduction. The broadband and tunable RCS reducing structure proposed in [95] employed

Table 4. Coding metasurfaces — Summary.

SI. No.	Ref. No.	Year	Working mechanism	a) Monostatic/bistatic b) RCS reduction frequency range (fractional bandwidth) c) Angular range if reported		Array size	Unit cell size
				Simulated	Measured		
1	[80]	2015	Diffused scattering	a) Monostatic/bistatic b) 0.8 to 1.4 THz c) 40 degrees	a) Monostatic/bistatic 0.5 to 1.8 THz c)40 degrees	$36.7\lambda_0 \times 36.7\lambda_0$	$0.40\lambda_0 \times 0.40\lambda_0$
2	[81]	2015	Diffused scattering	a) Monostatic/bistatic b) 0.8 to 2 THz c) 80 degrees	a) Monostatic/bistatic b) 0.5 to 1.6 THz c) 60 degrees	$25.2\lambda_0 \times 25.2\lambda_0$	$0.30\lambda_0 \times 0.30\lambda_0$
3	[86]	2017	Diffused scattering	a) Monostatic/bistatic b) 5.4 to 7.4 GHz (31.25%)	a) Monostatic/bistatic b) 5.57 to 7.37 GHz (27.82%)	$7\lambda_0 \times 7\lambda_0$	$0.11\lambda_0 \times 0.11\lambda_0$
4	[87]	2017	Diffused scattering	a) Monostatic/bistatic b) 13.2 to 23.2 GHz (54.9%) c) 60 degrees	a) Monostatic/bistatic b) 12.2 to 23.4 GHz (62.9%) c) 45 degrees	$17\lambda_0 \times 17\lambda_0$	$0.36\lambda_0 \times 0.36\lambda_0$
5	[89]	2018	Diffused scattering	a) Monostatic b) 7 GHz to 20 GHz (96.3%)* * (7dB- 8.7 GHz–11.3 GHz)	a) Monostatic b) 7 GHz to 20 GHz (96.3%)* * (7dB- 8.7 GHz–11.3 GHz)	$7.5\lambda_0 \times 7.5\lambda_0$	$0.45\lambda_0 \times 0.45\lambda_0$
6	[88]	2018	Polarization conversion	a) Monostatic/bistatic b) 6–15 GHz (85.7%)	a) Monostatic/bistatic b) 5.8–15.5 GHz (90.8%)	$10.5\lambda_0 \times 10.5\lambda_0$	$0.35\lambda_0 \times 0.35\lambda_0$
7	[92]	2018	Diffused scattering	a) Monostatic b) 9 GHz–11 GHz.	a) Monostatic b) 9 GHz–11 GHz	$8.4\lambda_0 \times 8.4\lambda_0$	$0.23\lambda_0 \times 0.23\lambda_0$
8	[83]	2018	Destructive interference	a) Monostatic/bistatic b) 8.5 GHz to 13.5 GHz	a) Monostatic/bistatic b) 8.5 GHz to 13.5 GHz	$11\lambda_0 \times 11\lambda_0$	$0.48\lambda_0 \times 0.48\lambda_0$
9	[84]	2019	Diffused scattering	a) Monostatic b) 15 GHz to 40 GHz (91%)	a) Monostatic b) 15 GHz to 40 GHz (91%)	$29\lambda_0 \times 29\lambda_0$	$0.46\lambda_0 \times 0.46\lambda_0$
10	[85]	2019	Diffused scattering and polarization conversion	a) Monostatic b) 14.4–48.5 GHz (108%)	a) Monostatic b) 18.3–42.2 GHz (108%)	$26.6\lambda_0 \times 26.6\lambda_0$	$0.42\lambda_0 \times 0.42\lambda_0$
11	[62]	2019	Diffused scattering and polarization conversion	a) Monostatic/bistatic b) 5.1 to 22.1 GHz (125%)	a) Monostatic b) 4.8–22.8 GHz (131%)	$14.5\lambda0 \times 14.5\lambda_0$	$0.36\lambda_0 \times 0.36\lambda_0$
12	[90]	2020	Destructive interference	a) Monostatic/bistatic b) 6.4 to 30.1 GHz (129%)	a) Monostatic/bistatic b) 6.4 to 29.6 GHz (128%)	$13.6\lambda_0 \times 13.6\lambda_0$	$0.48\lambda_0 \times 0.48\lambda_0$

a hybrid mechanism of combining a high-index grating structure with a traditional Salisbury screen. Here, the lossy sheet is made of graphene. On illumination with a normal incidence plane wave, the Salisbury screen absorbs the incoming wave, while the high-index grating structure further reduces the backward scattering wave by generating high-order reflection beams, which broadens the RCS reduction bandwidth. Additionally, the graphene layers aid in tuning the surface resistance, thereby dynamically controlling the RCS reduction level.

4.5.2. Locally Tuned

Locally tuned metasurfaces change the reflection characteristics of the metasurface at the unit cell level. In [97], each unit cell in the metasurface was integrated with one PIN diode, realizing a single polarization binary-coded locally tuned metasurface. The coding matrix was optimized using a genetic algorithm. Multiple functionalities were achieved, such as diffusion, beam steering, and anomalous reflection using a field-programmable gate array (FPGA), as shown in Figure 13. An FPGA-based control board, placed at the back of the metasurface, is connected with each sub-metasurface through a fixable winding wire which performs real-time control of each unit cell in the metasurface.

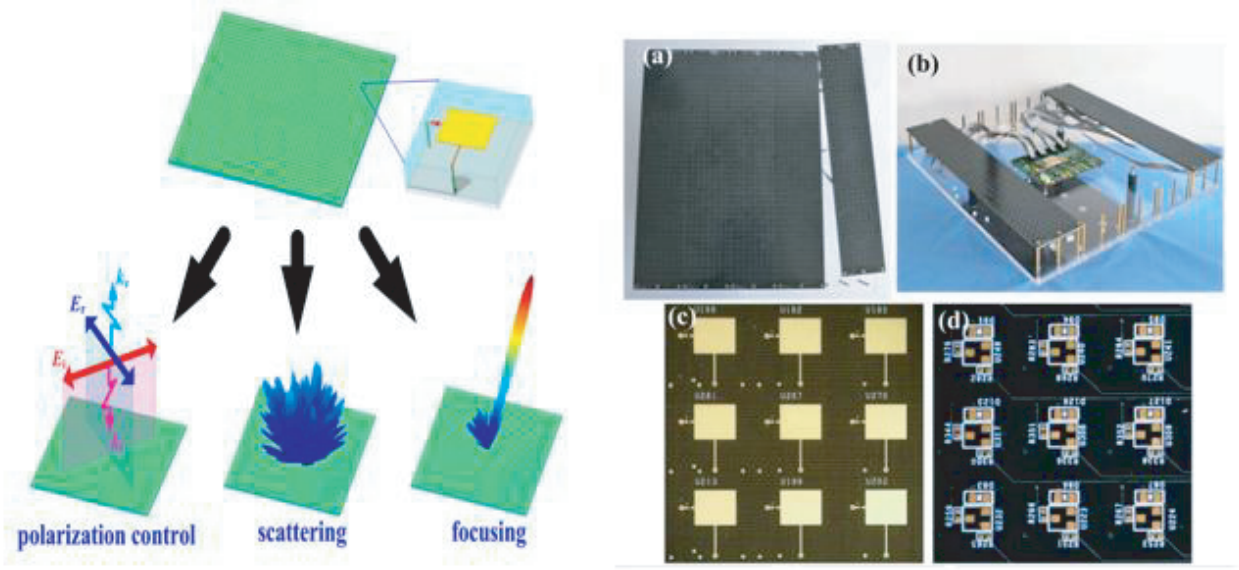

Figure 13. Programmable metasurfaces with different functionalities using FPGA, reproduced from [97].

Researchers have further integrated functionality at the metamaterial level. As the techniques progressed from passive to active, metasurfaces have been enhanced to dynamically and arbitrarily manipulate electromagnetic wavefields. However, manual intervention is required in the case of programmable metasurfaces to switch among different functionalities. A smart metasurface was designed to self-adaptively reprogram the functionalities by sensing ambient environments using a sensor. An automatic sensing feedback system is integrated to adjust its electromagnetic operational functionality adaptively. A motion-sensitive smart metasurface integrated with a three-axis gyroscope was reported in [98]; this metasurface can self-adaptively alter the electromagnetic radiation beams via different rotations of the metasurface. An online feedback algorithm is used to adaptively control the software switch between single-beam, multibeam steering, and other dynamic reactions.

4.6. Time-Varying Metasurfaces

The metasurfaces discussed above spatially manipulate the reflected waveform without disturbing the frequency content. Researchers are always keen to find new avenues to explore. One such enhancement is to spread the incident spectrum into a different frequency band that could aid in the non-detectability of the target. This is similar to time domain modulation or spread spectrum technologies and introduces a non-reciprocity to the functionality. A simple depiction illustrating the widespread of incident signals into different frequencies is shown in Figure 14, which is redrawn based on [99].

The time-varying metasurface presented in [100] breaks the Lorentz reciprocity concept to obtain time-varying characteristics. Metasurfaces used to manipulate electromagnetic scattering in the time

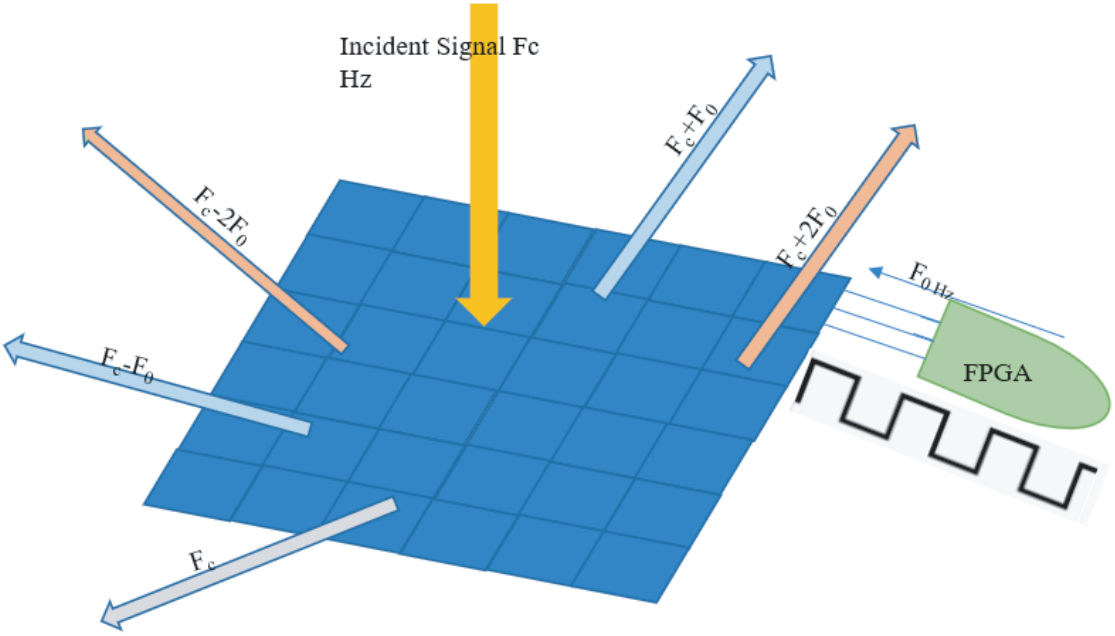

Figure 14. Illustration of time-varying metasurfaces, redrawn based on [99].

domain are termed time-varying metasurfaces [101]. The concept of a graded metasurface was extended by adding transverse temporal modulation of the surface impedance to attain the desired characteristics.

Space-time-modulated Huygens' metasurfaces were proposed in [102], emulating a travelling-type spatio-temporal perturbation using finite difference time domain (FDTD)-based numerical modeling. The FDTD-based modeling considers a set of second-order differential equations formulated by mapping the permittivity variation onto Lorentzian electric and magnetic susceptibility parameters. The obtained field solutions are solved using an explicit finite difference technique and integrated with a Yee cell-based propagation region to visualize the scattered fields.

Graphene-based time-varying metasurfaces that change the incident signal characteristics in the terahertz regime was reported in [103] and [104]. Graphene micro-ribbon arrays reported in [103] vary the Fermi level by doping the graphene, which induces time-varying changes in the complex refractive indices of graphene, resulting in active control of the reflection amplitude and phase. This causes Doppler-like shifts to control and manipulate light wave interactions actively.

In [105], a metasurface-based camouflaging technology was discussed using time-alternating PEC-PMC unit cell elements and pseudo-random time modulation. [99] employed complex modulation strategies to simultaneously tailor wave–matter interactions and the frequency spectrum, where discrete reflection phase states of the metasurface were controlled using digital-coding sequences. Non-linearity was employed by temporal modulation of incident waves on the metasurface by controlling the amplitude and phase distributions through external biasing voltages.

5. ABSORPTIVE METASURFACES FOR RCS REDUCTION

This section discusses RCS reduction achieved through absorption. Metasurface unit cells must satisfy two conditions to function as absorbers: (i) no reflection, and (ii) no transmission. The no reflection condition can be obtained by matching the absorbing layer impedance to that of free space. The transmission can be made zero either by increasing the absorbing layer thickness or by creating electromagnetic responses, utilizing both electric and magnetic field properties to dissipate the incident energy. The idea of a metamaterial-based absorber was proposed in [106]. Thin metasurfaces with resistive components coupled to the elements were reported in [107] and [108]. The perfect metamaterial

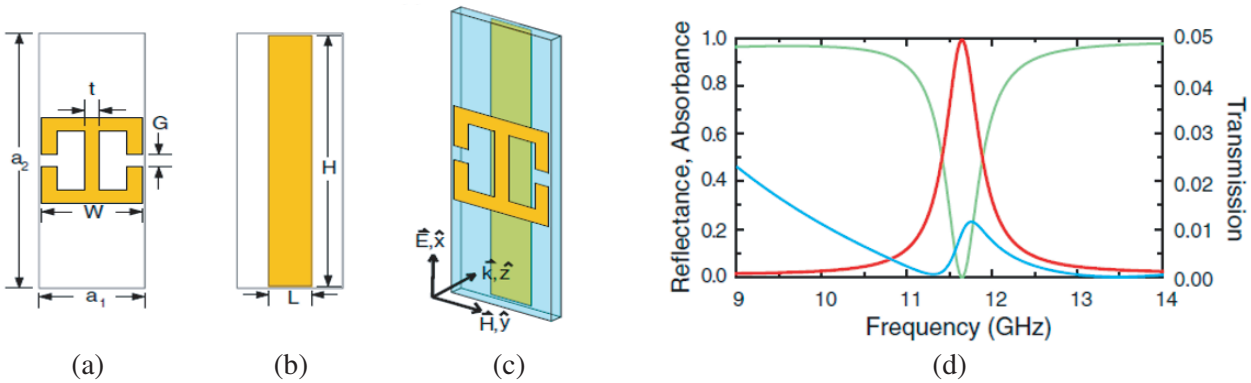

(a) (b) (c) (d)

Figure 15. Absorptive metasurfaces: (a) electric resonator, (b) cut wire, (c) unit cell, and (d) reflectance, transmittance and absorbance of the unit cell [109]. Reproduced with permission.

absorber presented in [109] offered more than 88% absorption at 11.5 GHz using the unit cell represented in Figure 15. [110] reported a metamaterial-based absorber with a thickness of $\lambda/4.7$ and 99.8% absorption over an 8% fractional bandwidth. The unit cell designed with no reflectance or transmittance at 10 GHz reported in [111] was applied to reduce the RCS of a metallic cube.

The functionality of the absorbers in [112] and [113] is explained through the surface current distribution. An ultra-wideband, ultra-thin X band absorber based on two concentric circular split rings has been described in [112], while a square ring-based triple X band absorber was explored in [113]. The surface current based design of the unit cells for absorption requires the surface currents over the elements to be anti-parallel to that in the ground plane. The multi-layer wideband circuit analogue absorber reported in [114] offers a fractional bandwidth of 114.4%. [115–117] report band-notched absorbers for wideband RCS reduction. A 3D metamaterial absorber made of the stand-up resistive film patch array [118] offers ultra-wideband absorption through the excitation of multiple standing wave modes, as well as from strong ohmic loss.

An equivalent circuit model of a square ring-based ultrathin metamaterial absorber was presented in [119]. It was modeled using a series of resonators connected in parallel with coupling capacitance and a short-circuited transmission line, as shown in Figure 16. The figure represents the even- and odd-mode couplings incorporated to accurately determine the lumped parameters and the absorption

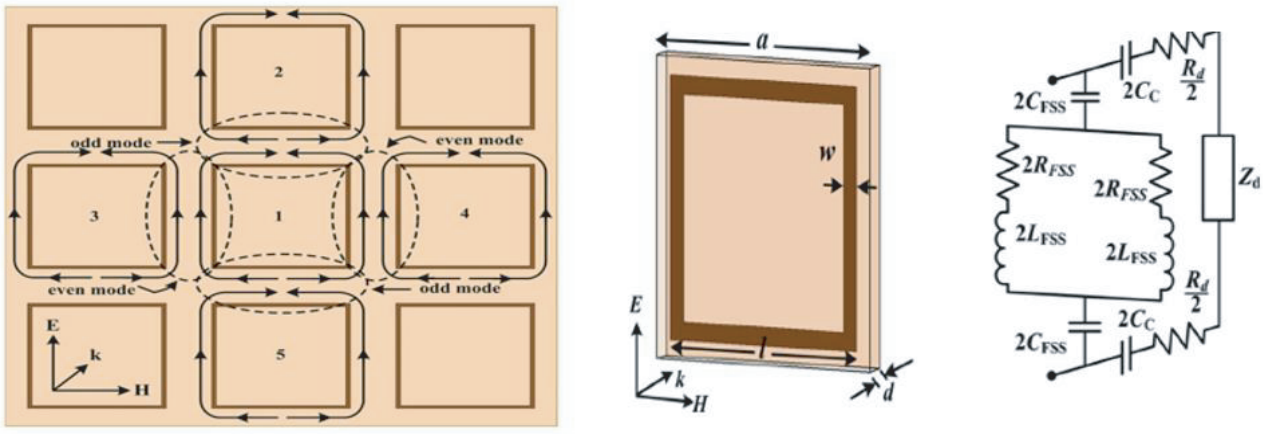

(a) (b) (c)

Figure 16. (a) Representation of even- and odd-mode coupling, (b) unit cell, and (c) equivalent circuit representation [119]. Reproduced with permission.

frequency of the absorber structure. Additional equivalent circuit model-based designs of metasurface absorbers were reported in [120–122]. A THz-range graphene-based absorber presented in [122] offered a bandwidth of 0.68 THz (0.79–1.47 THz).

It was demonstrated in [123] and [124] that magnetic loading increases the bandwidth of multiband AMC-based absorbers. A sugarcane bagasse-based composite absorber impacted by a frequency selective surface (FSS) layer had significantly improved microwave absorption characteristics [125]. A combination of metamaterial absorber and coding metasurface (ACM) in [126] further enhanced the

Table 5. Absorptive metasurfaces — A review.

SI. No	Ref. No.	Year	a) Monostatic/bistatic b) RCS reduction frequency range (fractional bandwidth) c) Angular range if reported		Array size	Unit cell size	Thickness
			Simulated	Measured			
1	[106]	2007	a) Monostatic b) 8–18 GHz (77%)	a) Monostatic b) 8–18 GHz (77%)	$6.9\lambda_0 \times 6.9\lambda_0$	$0.56\lambda_0 \times 0.56\lambda_0$	$0.138\lambda_0$
2	[111]	2013	a) Monostatic/bistatic b) 5.22 GHz, 7.44 GHz, 9.96 GHz, and 10.48 GHz c) 60 degrees	a) Monostatic/bistatic b) 5.258 GHz, 7.518 GHz, 10.02 GHz, and 10.494 GHz c) 60 degrees	$6.3\lambda_0 \times 6.3\lambda_0$	$0.47\lambda_0 \times 0.47\lambda_0$	$0.026\lambda_0$
3	[115]	2015	a) Monostatic b) 3.9 to 26.2 GHz (148%)	a) Monostatic b) 3.9 to 26.2 GHz	$12\lambda_0 \times 12\lambda_0$	$0.602\lambda_0 \times 0.602\lambda_0$	$0.55\lambda_0$
4	[112]	2015	a) Monostatic/bistatic b) 7.85 to 12.25 GHz (43%)	a) Monostatic/bistatic b) 8.08 to 12.12 GHz (40%)	$7.8\lambda_0 \times 7.8\lambda_0$	$0.238\lambda_0 \times 0.238\lambda_0$	$0.067\lambda_0$
5	[119]	2015	a) Monostatic b) 6.14 GHz	a) Monostatic b) 6.14 GHz	—	$0.204\lambda_0 \times 0.204\lambda_0$	$0.0204\lambda_0$
6	[114]	2016	a) Monostatic b) 5.1–18.08 (112%)	a) Monostatic b) 4.96–18.22 (114.40%)	$7\lambda_0 \times 7\lambda_0$	$0.502\lambda_0 \times 0.502\lambda_0$	$0.246\lambda_0$
7	[127]	2017	a) Monostatic/bistatic b) 4.893 to 5.55 GHz (10.94%) c) 60 degrees	a) Monostatic/bistatic b) 4.893 to 5.55 GHz (10.94%) c) 60 degrees	$5.3\lambda_0 \times 5.3\lambda_0$	$0.7\lambda_0 \times 0.7\lambda_0$	$0.028\lambda_0$
8	[120]	2018	a) Monostatic b) 5.9 GHz	a) Monostatic b) 5.9 GHz	$3.5\lambda_0 \times 3.5\lambda_0$	$0.39\lambda_0 \times 0.39\lambda_0$	$0.03\lambda_0$
9	[121]	2020	a) Monostatic/bistatic b) 1.98–9 GHz (119%) single layer 1.07–9.7 GHz (161%) double layer	a) Monostatic b) 1.98–9 GHz (119%) single layer 1.07–9.7 GHz (161%) double layer	–	$0.2745\lambda_0 \times 0.2745\lambda_0$ $0.302\lambda_0 \times 0.302\lambda_0$	$0.417\lambda_0$
10	[116]	2021	a) Monostatic b) 2.12 to 4.15 GHz (64%) 6.08 to 9.58 GHz (45%)	a) Monostatic b) 2.12 to 4.15 GHz (64%) 6.08 to 9.58 GHz (45%)	$5.7\lambda_0 \times 5.7\lambda_0$	$0.380\lambda_0 \times 0.380\lambda_0$	$0.234\lambda_0$
11	[117]	2021	a) Monostatic b) 2.48–5.23 (71.3%) 7.68–12.26 (45.9%)	a) Monostatic b) 2.48–5.23 (71.3%) 7.68–12.26 (45.9%)	–	$0.2457\lambda_0 \times 0.2457\lambda_0$	$0.2554\lambda_0$

RCS reduction bandwidth. The reported ACM showed a better RCS reduction performance than the individual metamaterial absorber or coding metasurface.

An absorber with high angular stability and reduced thickness was explored in [127]. Table 5 gives a comparative chart of the absorptive metasurfaces showing the features of RCS reduction bandwidth, size of the unit cell and the array, and the absorber's thickness.

All of the structures reported above reduce the RCS of flat metal targets while [128] reduces the RCS of antennas. All of the absorptive metasurfaces mentioned above are passive; however, [129] described an active liquid crystal metasurface tunable absorber that operates in the terahertz band and has a 30% amplitude tuned absorption and a frequency tunability of more than 4%. Active absorbers have also been applied to reduce the RCS of reflectarrays using a flexibly controllable model as reported in [130]. It has been designed such that the in-band phase profile of the reflecting surface constructively adds up to collimate the beam in the far-field while the out-of-band scattering from the reflector is significantly reduced.

6. FUTURE RESEARCH DIRECTIONS

RCS reduction bandwidth enhancement using scattering based metasurfaces has been achieved using multi-resonant elements [54], non-resonant elements [131] and elements that suppress surface waves [55]. Designs that are based on optimization algorithms enhances RCS reduction bandwidth, as can be seen, for example, in [46] and [89]. In [132], a rigorous Machine Learning-based framework for efficient design of low scattering metasurfaces is presented. It included modelling and optimization of AMC cells using a combination of global search, local refinement and direct local tuning of the entire metasurface. The approach resulted in CMS with broader bandwidth. A similar methodology can be applied to the design of other types of metasurfaces as well, as it may significantly improve the bandwidth performance.

As the tables show, the majority of the reported efforts have focused on monostatic characteristics. This gives rise to the question: do metasurfaces offering a broad monostatic bandwidth also offer similar bandwidth in bistatic situations? The answer to this would be no. The reason is that the surface impedance of the metasurface at oblique angles varies from that of the normal incidence, as can be explained based on Huygen's metasurfaces [133]. It has also been mentioned in [134] that inhomogeneous metasurfaces suffer degradation in performance when operating at oblique incidence due to inherent monochromatic aberrations. It is also demonstrated that beyond the monochromatic aberrations, the performance of the metasurface at oblique incidence is critically degraded by the angular dispersion of the meta-atoms. Hence it is essential to suppress this angular dispersion to achieve angularly stable elements, which can be attained by designing meta-atoms with minimum multi-polar mode coupling [134]. This type of element design clearly indicates that there is scope for expanding the investigations to bistatic RCS reduction.

The various factors responsible for wide bandwidth include element design, element spacing, the thickness of the metasurface and the overall size of the metasurface. Although these factors have been under continuous investigation for years for various electromagnetic problems, including antennas, it appears that the dependence of RCS reduction bandwidth on array size has not been explored. It has been reported, for phased arrays [135] and reflectarrays [136], that bandwidth depends on the array size. Undertaking studies on this aspect of RCS reduction dependence on the array size could probably lead to bandwidth enhancement.

Metasurfaces are also prone to mutual coupling — [44] and [57] — like any other array design, which leads to a degradation in performance.This opens up at least two avenues for exploration: (i) To enhance the RCS reduction bandwidth by mitigating mutual coupling effects [137], and (ii) To develop improved prediction models for array bandwidth from unit cell bandwidth [138]. Mutual coupling mitigation can be achieved using the following methods: (i) use of PEC walls such as baffles and vias [139] to reduce coupling between adjacent cells, and (ii) use of mutual coupling reduction techniques applied for MIMO antennas [140].

These are few areas that seem to attract the attention of the researchers.

7. CONCLUSION

This paper has reviewed the progression of various RCS reduction techniques, with a specific focus on metasurfaces. The two fundamental principles on which RCS reduction techniques work are scattering and absorption. A short review on shaping (scattering) and RAM (absorption), the traditional methods for reducing RCS, were first discussed. A comprehensive review of RCS reduction metasurfaces was then presented. Metasurfaces were also discussed in their passive and active configurations. The RCS reduction techniques are discussed with respect to their profile, bandwidth, angular stability, polarization sensitivity, design complexity, and cost-effectiveness. The metasurfaces are grouped with respect to operational principle, and its performance metrics such as bandwidth, size and angular stability are tabulated. Avenues that are open to further investigation are also discussed.

ACKNOWLEDGMENT

The authors thank Dr. C. Lakshmi, Department of English, SSN College of Engineering, for her assistance in proofreading the manuscript.

REFERENCES

1. "IEEE Standard for Radar Definitions," *IEEE Std 686-2017(Revision of IEEE Std 686-2008)*, 1–54, Sept. 13, 2017.
2. Knott, E. F., J. F. Shaeffer, and M. T. Tuley, *Radar Cross Section*, SciTech Pub, NC, 2004.
3. Dobrenz, L. T., A. Spadoni, and M. Jorgensen, "Aviation archeology of the horten 229 v3 aircraft," *10th AIAA Aviation Technology, Integration and Operations (ATIO) Conference*, Texas, 2010.
4. Ufimtsev, P. Y., "Method of edge waves in the physical theory of diffraction," *Soviet Radio*, Moscow, 1962.
5. Goodall, J. C., *Lockheed SR-71 Blackbird: The Illustrated History of America's Legendary Mach 3 Spy Plane*, Schiffer Publishing Ltd, 2018.
6. Yu, N. and F. Capasso, "Flat optics with designer metasurfaces," *Nature Materials*, 139–150, 2014.
7. Iyer, A. K., A. Alu, and A. Epstein, "Metamaterials and metasurfaces — Historical context, recent advances, and future directions," *IEEE Transactions on Antennas and Propagation*, Vol. 68, No. 3, 1223–1231, 2020.
8. Bukhari, S. S., Y. J. Vardaxoglou, and W. Whittow, "A metasurfaces review: Definitions and applications," *Applied Sciences*, Vol. 9, No. 13, 2019.
9. Chen, H.-T., A. J. Taylor, and N. Yu, "A review of metasurfaces: physics and applications," *Reports on Progress in Physics*, Vol. 79, No. 7, 2016.
10. Chen, M., M. Kim, A. M. H. Wong, and G. V. Eleftheriades, "Huygens' metasurfaces from microwaves to optics: A review," *Nanophotonics*, Vol. 7, No. 6, 1207–1231, 2018.
11. Fan, Y., J. Wang, X. Fu, Y. Li, Y. Pang, L. Zheng, M. Yan, J. Zhang, and S. Qu, "Recent developments of metamaterials/metasurfaces for RCS reduction," *EPJ Applied Metamaterials*, Vol. 6, No. 15, 2019.
12. Zaker, R. and A. Sadeghzadeh, "Passive Techniquesfor target radar cross section reduction: A comprehensive review," *International Journal of RF and Microwave Computer-Aided Engineering*, Vol. 30, No. 11, 2020.
13. Teruel, O. Q., H. Chen, A. Diaz Rubio, G. Gok, A. Grbic, G. Minatti, E. Martini, S. Maci, G. V. Eleftheriades, M. Chen, N. I. Zheludev, N. Papasimakis, S. Choudhury, Z. A. Kudyshev, S. Saha, H. Reddy, A. Boltasseva, V. M. Shalaev, V. A. Kildishev, D. Sievenpiper, C. Caloz, A. Alu, Q. He, L. Zhou, G. Valerio, E. Rajo-Iglesias, Z. Sipus, F. Mesa, R. R. Berral, F. Medina, V. Asadchy, S. Tretyakov and C. Craeye, "Roadmap on metasurfaces," *Journal of Optics*, Vol. 21, No. 7, 2019.

14. Maggiora, R., M. Saccani, and D. Milanesio, "An innovative harmonic radar to track flying insects: The case of vespa velutina," *Sci. Rep.*, Vol. 9, 2019.
15. Jeng, S.-L., W.-H. Chieng, and H.-P. Lu, "Estimating speed using a side-looking single-radar vehicle detector," *IEEE Transactions on Intelligent Transportation Systems*, Vol. 15, No. 2, 607–614, 2014.
16. Vinoy, K. J. and R. M. Jha, "Trends in radar absorbing materials technology," *Sadhana*, Vol. 20, 815–850, 1995.
17. Guo, W. L., K. Chen, G. M. Wang, X. Y. Luo, Y. J. Feng, and C. W. Qiu, "Transmission-Reflection-Selective metasurface and its application to RCS reduction of high-gain reflector antenna," *IEEE Transactions on Antennas and propagation*, Vol. 68, No. 3, 1426–1435, Mar. 2020.
18. Rao, G. A. and S. P. Mahulikar, "Integrated review of stealth technology and its role in airpower," *The Aeronautical Journal*, Vol. 106, 629–642, 1968.
19. Howe, D., "Introduction to the basic technology of stealth aircraft: Part 2 — Illumianation by the enemy (active considerations)," *ASME Journal of Engineering for Gas Turbine and Power*, Vol. 113, No. 75, 80–86, Jan. 1991.
20. Franscis, R. H., "The development of blue steel," *The Aeronautical Journal*, Vol. 68, No. 641, 303–322, 1964.
21. Bao, G. and J. Lai, "Optimal shape design of a cavity for radar cross section reduction," *SIAM Journal on Control and Optimization*, Vol. 52, No. 4, 2122–2140, 2014.
22. Peixoto, G. G., A. L. de Paula, L. A. Andrade, C. M. A. Lopes, and M. C. Rezende, "Radar Absorbing Material (RAM) and shaping on radar cross section reduction of dihedral corners," *SBMO/IEEE MTT-S International Conference on Microwave and Optoelectronics*, Brasilia, 2005.
23. Swandic, J. R., "Bandwidth limits and other considerations for monostatic RCS reduction by virtual shaping," Naval Surface Warfare Center, 2004.
24. Saville, P., "Review of radar absorbing materials," Defence R&D Canada, Atlantic, Dartmouth, 2005.
25. Ali, Z., B. Muneer, B. S. Chowdry, S. Jehangir, and G. Hyder, "Design of microwave pyramidal absorber for semi anechoic chamber in 1 GHz $\sim$ 20 GHz range," *International Journal of Wireless and Microwave Technologies*, Vol. 10, No. 2, 22–29, 2020.
26. Sweetman, B., "Stealth aircraft-history, technology and outlook," *Gas Turbine and Aeroengine Congress and Exposition*, Brussels, 1990.
27. Berenger, J. P., "A perfectly matched layer for the absorption of electromagnetic waves," *Journal of Computational Physics*, Vol. 114, No. 2, 185–200, 1994.
28. Salisbury, W. W., "Absorbent body for electromagnetic waves," US Patent 2599944, Jun. 10, 1952.
29. Chambers, B. and A. Tennant, "Optimized design of jaumann radar absorbing materials using a genetic algorithm," *IEE Proceedings — Radar, Sonar and Navigation*, Vol. 143, No. 1, 23–30, 1996.
30. Selvanayagam, M. and G. V. Eleftheriades, "Discontinuous electromagnetic fields usingorthogonal electric and magnetic currents for wavefront manipulation," *Optics Express*, Vol. 21, No. 12, 14409–14429, 2013.
31. Wong, J. P. S., M. Selvanayagam, and G. V. Eleftheriades, "Design of unit cells and demonstration of methods for synthesizing Huygens metasurfaces," *Photonics and Nanostructures — Fundamentals and Applications*, Vol. 12, No. 4, 360–375, 2014.
32. Pfeiffer, C. and A. Grbic, "Metamaterial Huygens' surfaces: Tailoring wave fronts with reflectionless sheets," *Physics Review Letters*, Vol. 110, No. 19, 197401, 2013.
33. Epstein, A. and G. V. Eleftheriades, "Shielded perfect reflectors based on omega-bianisotropic metasurfaces," *International Workshop on Antenna Technology: Small Antennas, Innovative Structures, and Applications (iWAT)*, Athens, Greece, 2017.
34. Selvanayagam, M. and G. V. Eleftheriades, "Polarization control using tensor Huygens surfaces," *IEEE Transactions on Antennas and Propagation*, Vol. 62, No. 12, 6155–6168, 2014.

35. Pfeiffer, C. and A. Grbic, "Bianisotropic metasurfaces for optimal polarization control: Analysis and synthesis," *Physical Review Applied*, 2014.
36. Yu, N. Y., P. Genevet, M. A. Kats, F. Aieta, J.-P. Tetienne, F. Capasso, and Z. Gaburro, "Light propagation with phase discontinuities: Generalized laws of reflection and refraction," *Science*, Vol. 334, No. 6054, 333–337, Oct. 21, 2011.
37. Sun, S., K.-Y. Yang, C.-M. Wang, T.-K. Juan, W. T. Chen, C. Y. Liao, D. He, S. Xiao, W.-T. Kung, G.-Y. Guo, L. Zhou, and D. P. Tsai, "High-efficiency broadband anomalous reflection by gradient metasurfaces," *Nano Letters*, Vol. 12, No. 12, 6223–6229, Nov. 28, 2012.
38. Sun, S., Q. He, S. Xiao, Q. Xu, X. Li, and L. Zhou, "Gradient-index meta-surfaces as a bridge linking propagating waves and surface waves," *Nature Materials*, Vol. 11, 426–431, 2012.
39. Pu, M., P. Chen, C. Wang, Y. Wang, Z. Zhao, C. Hu, C. Huang, and X. Luo, "Broadband anomalous reflection based on Gradient low-Q meta-surface," *AIP Advances*, Vol. 3, 052136, 2013.
40. Li, Y., J. Zhang, S. Qu, J. Wang, H. Chen, Z. Xu, and A. Zhang, "Wideband radar cross section reduction using two-dimensional phase gradient metasurface," *Applied Physics Letters*, Vol. 221110, 2014.
41. Chen, J., Q. Cheng, J. Zhao, D. S. Dong, and T. J. Cui, "Reduction of radar cross section based on a metasurface," *Progress In Electromagnetics Research*, Vol. 146, 71–76, 2014.
42. Cheng, Y., C. Wu, J. Yang, X. Peii, F. Jia, and R. Gong, "An ultra-thin dual-band phase-gradient metasurface using hybrid resonant structures for backward RCS reduction," *Applied Physics B*, Vol. 143, Apr. 18, 2017.
43. Zheng, Q., Y. Li, J. Zhang, J. Wang, H. Ma, Y. Pang, Y. Han, S. Sui, Y. Shen, H. Chen, and S. Qu, "Wideband, wide-angle coding phase gradient metasurfaces based on Pancharatnam-Berry phase," *Scientific Reports*, Vol. 7, 43543, 2017.
44. Azizi, Y., M. Soleimani, and S. H. Sedighy, "Ultra-wideband radar cross section reduction using amplitude and phase gradient modulated surface," *Journal of Applied Physics*, Vol. 128, No. 20, 2020.
45. Zhang, W., Y. Liu, S. Gong, J. Wang, and Y. Jiang, "Wideband RCS reduction of a slot array antenna using phase gradient metasurface," *IEEE Antennas and Wireless Propagation Letters*, Vol. 17, No. 12, 2193–2197, Dec. 2018.
46. Murugesan, A. and K. T. Selvan, "On further enhancing the bandwidth of wideband RCS reduction checkerboard metasurfaces using an optimization algorithm," *International Journal of RF and Microwave Computer-Aided Engineering*, Vol. 31, No. 7, e22686, 2021.
47. Paquay, M., J.-C. Iriarte, I. Ederra, R. Gonzalo, and P. D. Maagt, "Thin AMC structure for radar cross-section reduction," *IEEE Transactions on Antennas and Propagation*, Vol. 55, No. 12, 3630–3638, Dec. 2007.
48. De Cos, M. E., Y. Alvarez-Lopez, and F. L. H. Andres, "A novel approach for RCS reduction using a combination of artificial magnetic conductors," *Progress In Electromagnetics Research*, Vol. 107, 147–159, 2010.
49. Fu, Y., Y. Li, and N. Yuan, "Wideband composite AMC surfaces for RCS reduction," *Microwave and Optical Technology Letters*, Vol. 53, No. 4, 712–715, 2011.
50. Galarregyi, J. C. I., A. T. Pereda, J. L. M. D. Falcon, I. Ederra, R. Gonzalo, and P. D. Maagt, "Broadband radar cross-section reduction using AMC technoogy," *IEEE Transactions on Antennas and Propagation*, Vol. 61, No. 12, 6136–6143, 2013.
51. Chen, W., C. A. Balanis, and C. R. Britcher, "Checkerboard EBG surfaces for wideband radar cross section reduction," *IEEE Transactions on Antennas and Propagation*, Vol. 63, No. 6, 263–264, Jun. 2015.
52. Chen, W., C. A. Balanis, and R. C. Birtcher, "Dual wide-band checkerboard surfaces for radar cross section reduction," *IEEE Transactions on Antennas and Propagation*, Vol. 64, No. 9, 4133–4138, Sept. 2016.

53. Modi, A. Y., C. A. Balanis, C. R. Birtcher, and H. N. Shaman, "Novel design of ultrabroadband radar cross section reduction surfaces using artificial magnetic conductor," *IEEE Transactions on Antennas and Propagation*, Vol. 65, No. 10, 5406–5417, Oct. 2017.
54. Sang, D., Q. Chen, L. Ding, M. Guo, and Y. Fu, "Design of checkerboard AMC structure for wideband RCS reduction," *IEEE Transactions on Antennas and Propagation*, Vol. 67, No. 4, 2604–2012, Apr. 2019.
55. Kim, S. H. and Y. J. Yoon, "Wideband radar cross-section reduction on checkerboard metasurfaces with surface wave suppression," *IEEE Antenna and Wireless Propagation Letters*, Vol. 18, No. 5, 896–900, 2019.
56. Su, J., J. Lu, Y. Yang, Z. Li, and J. Song, "A novel checkerboard metasurface based on optimized multielement phase cancellation for superwideband RCS redcution," *IEEE Transaction on Antennas and Propagation*, Vol. 66, No. 12, 7091–7099, 2018.
57. Zaker, R. and A. Sadegnzadeh, "Wideband radar cross section reduction using a noveldesign of artificial magnetic conductor structure with a triple-layer configuration," *International Journal of RF and Microwave Computer-Aided Engineering*, Vol. 19, No. 2, e21545, Oct. 2018.
58. Modi, A. Y., C. A. Balanis, R. C. Britcher, and H. N. Shaman, "New class of RCS reduction metasurfaces based on scattering cancellation array theory," *IEEE Transactions on Antennas and Propagation*, Vol. 67, No. 1, 298–308, Jan. 2019.
59. Murugesan, A., D. Natarajan, and K. T. Selvan, "Low-cost, wideband checkerboard metasurface for monostatic RCS reduction," *IEEE Antennas and Wireless Propagation Letters*, Vol. 20, No. 4, 493–497, Apr. 2021.
60. Modi, A. Y., M. A. Alyahya, C. A. Balanis, and R. C. Birtcher, "Metasurface-based method for broadband RCS reduction of dihedral corner reflectors with multiple bounces," *IEEE Transactions on Antennas and Propagation*, Vol. 68, No. 3, 1436–1447, Mar. 2020.
61. Chen, W., C. A. Balanis, C. R. Birtcher, and A. Y. Modi, "Cylindrically curved checkerboard surfaces for radar cross-section reduction," *IEEE Antennas and Wireless Propagation Letters*, Vol. 17, No. 2, 343–346, Feb. 2018.
62. Akbari, M., F. Samadi, A.-R. Sebak, and T. A. Denidni, "Superbroadband diffuse wave scattering based on coding metasurfaces: Polarization conversion metasurfaces," *IEEE Antennas and Propagation Magazine*, Vol. 61, No. 2, 40–52, Apr. 2019.
63. Chen, H., J. Wang, H. Ma, S. Qu, Z. Xu, A. Zhang, M. Yan, and Y. Li, "Ultra-wideband polarization conversion metasurfaces based on multiple plasmon resonances," *Journal of Applied Physics*, Vol. 115, 2014.
64. Jiang, W., Y. Xue, and S.-X. Gong, "Polarization conversion metasurface for broadband radar cross section reduction," *Progress In Electromagnetics Research Letters*, Vol. 62, 9–15, 2016.
65. Jia, Y., Y. Liu, K. Li, and S.-X. Gong, "Broadband polarization rotation reflective surfaces and their applications to RCS reduction," *IEEE Transactions on Antennas and Propagation*, Vol. 64, No. 1, 179–188, Jan. 2016.
66. Sun, H., C. Gu, X. Chen, L. Liu, B. Xu, and Z. Zhou, "Broadband and broad-angle polarization-independent metasurface for radar cross section reduction," *Scientific Reports*, Vol. 7, Jan. 20, 2017.
67. Jia, Y., Y. Liu, J. Y. Guo, K. Li, and S. Gong, "A dual-patch polarization rotation reflective surface and its application to ultra-wideband RCS reduction," *IEEE Transactions on Antennas and Propagation*, Vol. 65, No. 6, 3291–3295, Jun. 2017.
68. Ameri, E., S. H. Esmaeli, and S. H. Sedighy, "Ultra wideband radar cross section reduction by using polarization conversion metasurfaces," *Scientific Reports*, Vol. 9, Jan. 24, 2019.
69. Yang, J. J., Y. Z. Cheng, C. C. Ge, and R. Z. Gong, "Broadband polarization conversion metasurface based on metal cut-wire structure for radar cross section reduction," *Materials*, Vol. 11, No. 4, 626, 2018.
70. Rajabalipanah, H. and A. Abdolali, "Ultrabroadband monostatic/bistatic RCS reduction via high-entrophy phase-encoded polarization conversion metasurfaces," *IEEE Antennas and Wireless Propagation Letters*, Vol. 18, No. 6, 1233–1237, Jun. 2019.

71. Dai, H., Y. Zhao, J. Chen, C. Yu, and L. Xing, "Ultra-wideband radar cross-section reduction using polarization conversion metasurface," *International Journal of RF and Microwave Computer-Aided Engineering*, e22085, Dec. 11, 2019.
72. Fu, C., L. Han, C. Liu, Z. Sun, and X. Lu, "Dual-band polarization conversion metasurface for RCS reduction," *IEEE Transactions on Antennas and Propagation*, Vol. 69, No. 5, 3044–3049, May 2021.
73. Long, M., W. Jiang, and S. Gong, "Wideband RCS reduction using polarization conversion metasurface and partially reflecting surface," *IEEE Antennas and Wireless Propagation Letters*, Vol. 16, 2534–2537, 2017.
74. Sun, S., W. Jiang, X. Li, P. Liu, and S. Gong, "Ultrawideband high-efficiency 2.5-dimensional polarization conversion metasurface and its application in RCS reduction of antenna," *IEEE Antenna and Wireless Propagation Letters*, Vol. 18, No. 5, 881–885, 2019.
75. Hong, T., S. Wang, Z. Liu, and S. Gong, "RCS reduction and gain enhancement for the circularly polarized array by polarization conversion metasurface coating," *IEEE Antennas and Wireless Propagation Letters*, Vol. 18, No. 1, 167–171, Jan. 2019.
76. Liu, Y., K. Li, Y. Jia, Y. Hao, S. Gong, and Y. J. Guo, "Wideband RCS reduction of a slot array antenna using polarization conversion metasurface," *IEEE Transactions on Antennas and Propagation*, Vol. 64, No. 1, 326–331, Jan. 2016.
77. Qi, Y., B. Zhang, C. Li, and X. Deng, "Ultra-broadband polarization conversion meta-surface and its application in polarization converter and RCS reduction," *IEEE Access*, Vol. 8, 116675–116684, 2010.
78. Giovampaola, C. D. and N. Engheta, "Digital metamaterials," *Nature Materials*, Vol. 13, 1115–1121, 2014.
79. Cui, T. J., M. Q. Qi, X. Wan, J. Zhao, and Q. Cheng, "Coding metamaterials, digital metamaterials and programmable metamaterials," *Light: Science and Applications*, Vol. 3, 218, 2014.
80. Liang, L., M. Qi, J. Yang, X. Shen, J. Zhai, W. Xu, B. Jin, W. Liu, Y. Feng, C. Zhang, H. Lu, H.-T. Chen, L. Kang, W. Xu, J. Chen, T. J. Cui, P. Wu, and S. Liu, "Anomalous terahertz reflection and scattering by flexible and conformal coding metamaterials," *Advanced Optical Materials*, 2015.
81. Gao, L.-H., Q. Cheng, J. Yang, S.-J. Ma, J. Zhao, S. Liu, H.-B. Chen, Q. He, W.-X. Jiang, H.-F. Ma, Q.-Y. Wen, L.-J. Liang, B.-B. Jin, W.-W. Liu, L. Zhou, J.-Q. Yao, P.-H. Wu, and T.-J. Cui, "Broadband diffusion of terahertz waves by multi-bit coding metasurfaces," *Light: Science and Applications*, Vol. 4, 2015.
82. Liu, S., T. J. Cui, Q. Xu, D. Bao, L. Du, X. Wan, W. X. Tang, C. Ouyang, X. Y. Zhou, H. Yuan, F. H. Ma, W. X. Jiang, J. Han, W. Zhang, and Q. Cheng, "Anisotropic coding metamaterials and their powerful manipulation of differently polarized terahertz waves," *Light: Science and Applications*, Vol. 5, 2016.
83. Li, F.-F., W. Fang, P. Chen, Y. Poo, and R.-X. Wu, "Transmission and radar cross-section reduction by combining binary coding metasurface and frequency selective surface," *Optics Express*, Vol. 26, No. 26, 33878–33887, 2018.
84. Saifullah, Y., A. B. Waqas, G.-M. Yang, F. Zhang, and F. Xu, "4-bit optimized coding metasurface for wideband RCS reduction," *IEEE Access*, Vol. 7, 122378–122386, 2019.
85. Dai, H., Y. Zhao, H. Li, J. Chen, Z. He, and W. Qi, "An ultra-wide band polarization-independent random coding metasurfaces for RCS reduction," *Electronics*, Vol. 8, No. 10, 2019.
86. Liu, X., J. Gao, L. Xu, Y. Zhao, X. Cao, and S. Li, "A coding diffuse metasurface for RCS reduction," *IEEE Antennas and Wireless Propagation Letters*, Vol. 16, 724–727, 2016.
87. Yuan, F., G. M. Wang, H. X. Xu, T. Cai, X. J. Zou, and Z. H. Pang, "Broadband RCS reduction based on spiral-coded metasurface," *IEEE Antennas and Wireless Propagation Letters*, Vol. 16, 3188–3191, 2017.
88. Yang, J. J., Y. Z. Cheng, D. Qi, and R. Z. Gong, "Study of energy scattering relation and RCS reduction characteristic of matrix-type coding metasurface," *Applied Sciences*, Vol. 8, No. 8, 2018.

89. Jidi, L., X. Cao, Y. Tang, S. Wang, Y. Zhao, and X. Zhu, "A new coding metasurface for wideband RCS reduction," *Radio Engineering*, Vol. 27, No. 2, 2018.
90. Wu, G., W. Yu, T. Lin, Y. Deng, and J. Liu, "Ultra-wideband RCS reduction based on non-planar coding diffusive metasurface," *Materials*, Vol. 13, No. 21, 2020.
91. Chen, K., L. Cui, Y. Feng, J. Zhao, T. Jiang, and B. Zhu, "Coding metasurface for broadband microwave scattering reduction with optical transparency," *Optics Express*, Vol. 25, No. 5, 5571–5579, 2017.
92. Swain, R. and R. K. Mishra, "Phase quantized metasurface supercells for wave manipulation and RCS reduction," *Progress In Electromagnetics Research M*, Vol. 74, 125–135, 2018.
93. Li, X., M. Feng, J. Wang, Y. Meng, J. Yang, T. Liu, R. Zhu, and S. Qu, "Suppressing edge back-scattering of electromagnetic waves using coding metasurface purfle," *Frontier in Physics*, 2020.
94. Sheng, L. J., L. S. He, and Y. J. Quan, "Actively tunable terahertz coding metasurfaces," *Optics Communications*, Vol. 461, 2020.
95. Song, J., X. Wu, C. Huang, J. Yang, C. Ji, C. Zhang, and X. Luo, "Broadband and tunable RCS reduction using high-order reflections and salisbury-type absorption mechanisms," *Scientific Reports*, Vol. 9, 2019.
96. Liu, S. and T. J. Cui, "Flexible controls of terahertz waves using coding and programmable metasurfaces," *IEEE Journal of Selected Topics in Quatum Electronics*, Vol. 23, No. 4, 1–12, 2017.
97. Yang, H., X. Cao, F. Yang, J. Gao, S. Xu, M. Li, X. Chen, Y. Zhao, Y. Zheng, and S. Li, "A programmable metasurface with dynamic polarization, scattering and focusing control," *Scientific Reports*, Vol. 6, 2016.
98. Ma, Q., G. D. Bai, H. B. Jing, C. Yang, L. Li, and T. J. Cui, "Smart metasurface with self-adaptively reprogrammable functions," *Light: Science & Applications*, Vol. 8, 2019.
99. Zhao, J., X. Yang, J. Y. Dai, Q. Cheng, X. Li, N. H. Di, J. C. Ke, G. D. Bai, S. Liu, and S. Jin, "Programmable time-domain digital-coding metasurface for non-linear harmonic manipualtion and new wireless communication systems," *National Science Review*, Vol. 6, No. 2, 231–238, 2019.
100. Shaltout, A., A. Kildishev, and V. Shalaev, "Time-varying metasurfaces and Lorentz non-reciprocity," *Optical Materials Express*, Vol. 5, No. 11, 2459–2467, 2015.
101. Liu, M., A. B. Kozyrev, and I. V. Shadrivov, "Time-varying metasurfaces for broadband spectrral camouflage," *Phys. Rev. Applied*, Vol. 12, No. 5, 054052–054060, 2019.
102. Stewart, S. A., T. J. Smy, and S. Gupta, "Finite-difference time-domain modeling of space-time-modulated metasurfaces," *IEEE Transactions on Antennas and Propagation*, Vol. 66, No. 1, 281–292, 2018.
103. Liu, Z., Z. Li, and K. Aydin, "Time-varying metasurfaces based on graphene microribbon arrays," *ACS Photonics*, Vol. 3, No. 11, 2035–2039, 2016.
104. Salary, M. M., S. J. Zanjani, and H. Mosallaei, "Time-varying metamaterials based on graphene-wrapped microwires: Modeling and potential applications," *Phys. Rev. B*, Vol. 97, No. 11, 115421–115435, 2018.
105. Wang, X. and C. Caloz, "Spread-spectrum selective camouflaging based on time-modualted metasurface," *IEEE Transactions on Antennas and Propagation*, Vol. 69, No. 1, 286–295, 2021.
106. Engheta, N., "Thin absorbing screens using metamaterial surfaces," *IEEE Antennas and Propagation Society International Symposium*, San Antonio, TX, USA, 2002.
107. Mosallaei, H. and K. Sarabandi, "A one-layer ultra-thin meta-surface absorber," *IEEE Antennas and Propagation Society International Symposium*, Washington, DC, USA, 2005.
108. Yang, J. and Z. Shen, "A thin and broadband absorber using double-square loops," *IEEE Antennas and Wireless Propagation Letters*, Vol. 6, 388–391, 2007.
109. Landy, N. I., S. Sajuyigbe, J. J. Mock, D. R. Smith, and W. J. Padilla, "Perfect metamaterial absorber," *Phys. Rev. Lett.*, Vol. 100, No. 20, 207402–207406, 2008.

110. Alici, K. B., F. Bilotti, L. Vegni, and E. Ozbay, "Experimental verification of metamaterial based subwavelength microwave absorbers," *Journal of Applied Physics*, Vol. 108, No. 8, 2010.
111. Assimonis, A. D., T. M. Kollatou, T. V. Yioultsis, and C. S. Antonopoulos, "Absorbing surfaces using EBG structures," *IEEE Transactions on Magnetics*, Vol. 50, No. 2, 197–200, 2014.
112. Ghosh, S., S. Bahttacharyya, D. Chaurasiya, and K. V. Srivastava, "An ultrawideband ultrathin metamaterial absorber based on circular split rings," *IEEE Antennas and Wireless Propagation Letters*, Vol. 14, 1172–1175, 2015.
113. Bhattacharyya, S., S. Ghosh, and K. V. Srivastava, "Triple band polarizaion-independent metamaterial absorber with bandwidth enhancement at X-band," *Journal of Applied Physics*, Vol. 114, No. 9, 2013.
114. Ghosh, S., S. Bhattacharyya, and K. V. Srivastava, "Design, characterisation and fabrication of a broadband polarisation-insensitive multi-layer circuit analogue absorber," *IET Microwaves, Antennas & Propagation*, Vol. 10, No. 8, 850–855, 2016.
115. Han, Y., L. Zhu, Y. Chang, and B. Li, "Dual-polarized bandpass and band-notched frequency-selective absorbers under multimode resonance," *IEEE Transactions on Antennas and Propagation*, Vol. 66, No. 12, 7449–7454, 2018.
116. Sharma, A., S. Ghosh, and K. V. Srivastava, "A polarization-insensitive band-notched absorber," *IEEE Antennas and Wireless Propagation Letters*, Vol. 20, No. 2, 259–263, 2021.
117. Sharma, A., S. Malik, S. Ghosh, and K. V. Srivastava, "A miniaturized band-notched absorber for wideband RCS reduction," *2020 International Symposium on Antennas and Propagation*, Osaka, Japan, 2020.
118. Shen, Y., Z. Pei, Y. Pang, J. Wang, A. Zhang, and S. Qu, "An extremely wideband and lightweight metamaterial absorber," *Journal of Applied Physics*, Vol. 117, No. 22, 2015.
119. Ghosh, S. and K. V. Srivastava, "An equivalent circuit model of FSS-based metamaterial absorber using coupled line theory," *IEEE Antennas and Wireless Propagation Letters*, Vol. 14, 511–514, 2014.
120. Kundu, D., A. Mohan, and A. Chakrabarty, "Design of a conductive FSS based ultrathin absorber using impedance analysis method of equivalent circuit model," *IEEE Indian Conference on Antennas and Propagation*, 2018.
121. Hossain, M. I., N. Nguyen-Trong, K. H. Sayidmarie, and A. M. Abbosh, "Equivalent circuit design method for wideband nonmagnetic absorbers at low microwave frequencies," *IEEE Transactions on Antennas and Propagation*, Vol. 68, No. 12, 8215–8220, 2020.
122. Mishra, R., R. Panwar, and D. Singh, "Equivalent circuit model for the design of frequency-selective, terahertz-band, graphene-based metamaterial absorbers," *IEEE Magnetic Letters*, Vol. 9, 1–5, 2018.
123. Kern, D. J. and D. H. Werner, "Magnetic loading of EBG AMC ground planes and ultrathin absorbers for improved bandwidth performance and reduced size," *Microwave Optical Letters*, Vol. 48, No. 12, 2468–2471, 2006.
124. Deng, T., Z.-W. Li, and Z. N. Chen, "Ultrathin broadband absorber using frequency-selective surface and frequency-dispersive magnetic materials," *IEEE Transactions on Antennas and Propagation*, Vol. 65, No. 11, 5886–5894, 2017.
125. Panwar, R., S. Puthucheri, D. Singh, V. Agarwala, and J. R. Lee, "Microwave absorption properties of FSS-impacted composites as a broadband microwave absorber," *Advanced Composite Materials*, Vol. 26, No. 2, 99–113, 2016.
126. Sui, S., H. Ma, J. Wang, Y. Pang, M. Feng, Z. Xu, and S. Qu, "Absorptive coding metasurface for further radar cross section reduction," *Journal of Physics D: Applied Physics*, Vol. 51, No. 6, 2018.
127. Mol, L. V. A. and C. K. Anandan, "An ultrathin microwave metamaterial absorber with enhanced bandwidth and angular stability," *Journal of Physics Communication*, Vol. 1, No. 1, 2017.

128. Huang, H., Z. Shen, and A. A. Omar, "3-D absorptive frequency selective reflector for antenna radar cross section reduction," *IEEE Transactions on Antennas and Propagation*, Vol. 65, No. 11, 5908–5917, 2017.
129. Shrekenhamer, D., W.-C. Chen, and W. J. Padilla, "Liquid crystal tunable metamaterial absorber," *Physical Review Letters*, Vol. 110, 2013.
130. Huang, H. and Z. Shen, "Low-RCS reflectarray with phase controllable absorptive frequency-selective reflector," *IEEE Transactions on Antennas and Propagation*, Vol. 67, No. 1, 190–198, 2019.
131. Wang, Y., K. Chen, Y. Li, and Q. Cao, "Design of nonresonant metasurfaces for broadband RCS reduction," *IEEE Antennas and Wireless Propagation Letters*, Vol. 20, No. 3, 346–350, 2021.
132. Koziel, S. and M. Abdullah, "Machine-learning-powered EM-based framework for efficient and reliable design of low scattering metasurfaces," *IEEE Transactions on Microwave Theory and Techniques*, Vol. 69, No. 4, 2028–2041, 2021.
133. Wong, J. P. S., A. Epstein, and G. V. Eleftheriades, "Reflectionless wide-angle refracting metasurfaces," *IEEE Antennas and Wireless Propagation Letters*, Vol. 15, 1293–1296, 2015.
134. Fathnan, A. A., T. M. Hossain, D. Mahmudin, Y. N. Wijayanto, and A. D. Powell, "Characterization of broadband focusing microwave metasurfaces at oblique incidence," *Applied Physics*, 1–9, 2020.
135. Haupt, R. L., "Factors that define the bandwidth of a phased array antenna," *2019 IEEE International Symposium on Phased Array System & Technology (PAST)*, Waltham, MA, USA, 2019.
136. Shaker, J., M. R. Chacharmir, and J. Ethier, *Reflectarray Antennas Analysis, Design, Fabrication, and Measurement*, Artech House, Boston, London, 2014.
137. Murugesan, A. R. A. N. J. and K. T. Selvan, "Bandwidth enhancement of RCS reduction checkerboard metasurfaces by mutual coupling mitigation," *2021 International Applied Computational Electromagnetics Society (ACES) Symposium*, 2021.
138. Murugesan, A. and K. T. Selvan, "Toward improved prediction of RCS reduction bandwidth of checkerboard metasurfaces," accepted in *IEEE International Symposium on Antennas and Propagation and USNC-URSI Radio Science Meeting*, Marina Bay Sands, Singapore, 2021.
139. Xu, G., S. V. Hum, and G. V. Eleftheriades, "Augmented Huygens' metasurfaces employing baffles for precise control of wave transformations," *IEEE Transactions on Antennas and Propagation*, Vol. 67, No. 11, 6935–6946, 2019.
140. Nadeem, I. and D. Y. Choi, "Study on mutual coupling reduction technique," *IEEE Access*, Vol. 7, 563–586, 2019.